Published in final edited form as:

Cell Rep. 2022 July 12; 40(2): 111063. doi:10.1016/j.celrep.2022.111063.

Structural basis for acyl chain control over glycosphingolipid sorting and vesicular trafficking

Stefanie S. Schmieder[1], **Raju Tatituri**[2,3], **Michael Anderson**[1,4], **Kate Kelly**[1], **Wayne I. Lencer**[1,3,4,5,*]

[1]Division of Gastroenterology, Boston Children's Hospital, Boston, MA 02115, USA

[2]Division of Rheumatology, Brigham and Women's Hospital, Boston, MA 02115, USA

[3]Harvard Medical School, Boston, MA 02115, USA

[4]Harvard Digestive Diseases Center, Boston, MA 02115, USA

[5]Lead contact

SUMMARY

The complex sphingolipids exhibit a diversity of ceramide acyl chain structures that influence their trafficking and intracellular distributions, but it remains unclear how the cell discerns among the different ceramides to affect such sorting. To address the mechanism, we synthesize a library of GM1 glycosphingolipids with naturally varied acyl chains and quantitatively assess their sorting among different endocytic pathways. We find that a stretch of at least 14 saturated carbons extending from C1 at the water-bilayer interface dictate lysosomal sorting by exclusion from endosome sorting tubules. Sorting to the lysosome by the C14* motif is cholesterol dependent. Perturbations of the C14* motif by unsaturation enable GM1 entry into endosomal sorting tubules of the recycling and retrograde pathways independent of cholesterol. Unsaturation occurring beyond the C14* motif in very long acyl chains rescues lysosomal sorting. These results define a structural motif underlying the membrane organization of sphingolipids and implicate cholesterol-sphingolipid nanodomain formation in sorting mechanisms.

Graphical abstract

*Correspondence: wayne.lencer@childrens.harvard.edu.

AUTHOR CONTRIBUTIONS

S.S.S. and W.I.L. conceived the study; S.S.S., R.T., and W.I.L. designed the experiments and resources; S.S.S., R.T., and K.K. performed the experiments; S.S.S., R.T., and M.A. analyzed the data; and S.S.S. and W.I.L. wrote the manuscript.

SUPPLEMENTAL INFORMATION

Supplemental information can be found online at https://doi.org/10.1016/j.celrep.2022.111063.

DECLARATION OF INTERESTS

W.I.L. is founder and temporary board member of Transcera, which seeks to translate the trafficking of glycosphingolipids to clinical applications. He holds patent no. 9,457,097, and has applied for patents on 3 other products related to the mucosal delivery of therapeutic molecules, proteins, or particles coupled to ceramide lipids and short-chain ceramide-based lipids. The other authors declare no competing interests.

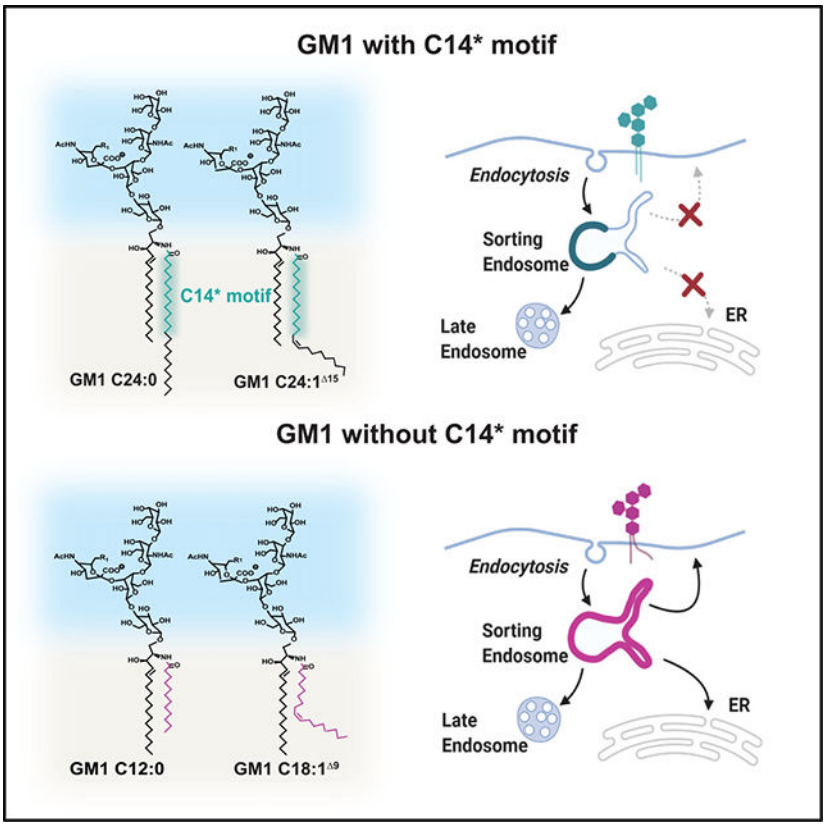

In brief

Lipids display structural diversity in their acyl chains. To elucidate the effect this diversity has on lipid trafficking, Schmieder et al. synthesize a glycosphingolipid (GM1) library with varied fatty acids. They find that GM1 is endosomally sorted by a C14* motif within the fatty acid of the ceramide moiety.

INTRODUCTION

Membrane function depends on the structural variations and dynamic physical properties of the acyl chains that form each class of its lipid components. However, how the acyl chains operate to differentially affect the membrane biology of a lipid and why so many different acyl chain structures are conserved within each lipid species remain in large part unexplained.

The complex sphingolipids, comprising the glycosphingolipids (GSLs) and sphingomyelin (SM), constitute 10–20 mol % of plasma membrane (PM) lipids (Koval and Pagano, 1991; van Meer and Simons, 1982), and they provide a tractable experimental system to examine how acyl chain structure affects lipid function. In many cases, the activities of complex glycosphingolipids appear to depend upon locally segregating into liquid-liquid phase-separated nanodomains that form upon close interactions with cholesterol (Brown and London, 1998; Chiantia and London, 2013; London, 2005; Ramstedt and Slotte, 2002), the cortical cytoskeleton (Day and Kenworthy, 2012; Fujita et al., 2009; Goswami et al., 2008;

Gowrishankar et al., 2012; Kusumi et al., 2012), and other scaffolding proteins (Johannes et al., 2015; Pike, 2004). This is the lipid-raft or lipid-nanodomain hypothesis (Jacobson et al., 2019; Lingwood and Simons, 2010; Raghunathan and Kenworthy, 2018; Sezgin et al., 2017; Simons and Sampaio, 2011; Simons and van Meer, 1988). Considerable evidence shows that nanodomains are critical for key cellular processes, including membrane protein trafficking, signal transduction, and receptor cell surface distributions (Deng et al., 2016; Garcia-Parajo et al., 2014; Jacobson et al., 2019; Lippincott-Schwartz and Phair, 2010; Patterson et al., 2008; Stone et al., 2017; Varshney et al., 2016; Zhou and Hancock, 2015). Because of their functions in vesicular trafficking, some GSLs forming membrane nanodomains are co-opted by viruses, bacterial toxins, and endogenous lectins, as platforms for entry into the cell and causation of disease (Campanero-Rhodes et al., 2007; Cuatrecasas, 1973; Lakshminarayan et al., 2014; Lencer and Tsai, 2003; Lorizate et al., 2013; Römer et al., 2007; Sandvig, 2001).

Here, we studied ganglioside GM1, the glycosphingolipid receptor that mediates cholera toxin (CTx) entry into host cells. GM1 typifies the complex sphingolipids in basic structure and function. The different GM1 species, like all other complex sphingolipids, comprise a hydrophilic extracellular moiety (a specific pentasaccharide for GM1, one or more sugars for the other GSLs, and phosphocholine for SM) coupled to a ceramide that anchors the molecule in the membrane. The ceramide moieties consist of a sphingosine base (predominantly 18 hydrocarbons long, C18:1$^{\Delta 4}$, *trans*) linked to a fatty acid by an amide bond to the C1 carbon positioned at the lipid bilayer-water interface. The sphingosine base varies in structure only to a small degree, but the acyl chain can display considerable heterogeneity in both length (C14–C26) and saturation (single *cis* or no double bond) (Hannun and Obeid, 2018; Merrill, 2011). Because these lipids contain large hydrophilic extracellular head groups, they are trapped in the outer leaflet of the membrane bilayer, and their distribution throughout the cell occurs only by vesicular traffic (van Meer et al., 2008; Young et al., 1992). This can be quantitatively measured and compared for GM1 species with identical head groups but with varied acyl chains in their ceramide moieties.

We previously found the different acyl chains in the ceramide moiety of GM1 act decisively in trafficking the toxin into the different endocytic and subcellular compartments required for the induction of toxicity (Chinnapen et al., 2012; Saslowsky et al., 2013). GM1 species containing ceramides with “kinked” shapes caused by a *cis*-double bond in the acyl chains (C16:1$^{\Delta 9}$ or C18:1$^{\Delta 9}$) sorted into the recycling and retrograde endosome pathways, and GM1 species containing ceramides with saturated acyl chains of the same length, C16:0 and C18:0, but with “straight” shapes, sorted to the lysosome instead (Chinnapen et al., 2012). Additional evidence that the acyl chain structure of the complex sphingolipids may affect trafficking was recently shown for ceramide-anchored proteins in the biosynthetic pathway of yeast (Rodriguez-Gallardo et al., 2020). How the cell discerns among the different ceramide moieties to affect this acyl chain-based sorting has not been explained.

To address these problems, we synthesized a library of 11 GM1 species with ceramides reflecting the naturally occurring variations of fatty acyl chain length and saturation. This provided a direct test of GSL structural biology in ways that were not previously possible.

Our structural analysis was based on an experiment provided by nature. In mammals, the single *cis*-double bond in the acyl chain of the unsaturated ceramide is created by palmitoyl/stearoyl-coenzyme A (CoA) desaturase (SCD). The enzyme installs a *cis*-double bond invariably at the Δ^9-position of C16:0 or C18:0 fatty acids, creating a "kinked"-shaped lipid. When coupled to sphingosine by the ceramide synthases, and then incorporated into the complex sphingolipids, the kink in the acyl chain of these ceramide species is positioned where it should impair close packing against the rigid planar surface of cholesterol (Ramstedt and Slotte, 1999). However, GSL species containing ceramides with longer unsaturated acyl chains will have the *cis*-double bonds placed deeper within the membrane bilayer. They are built upon the same C18:1 acyl chains generated by the Δ9-desaturase, but lengthened at the carboxyl terminus by the elongation of very-long-chain fatty acids (ELOVL) elongases (Kihara, 2012). Consequently, these unsaturated very long acyl chains contain longer stretches of saturated hydrocarbons extending from the water-bilayer interface into the membrane bilayer. In some cases, the *cis*-double bond will be positioned beyond the planar surface of cholesterol. We reasoned that these unsaturated and kinked very long acyl chain GSLs may still assemble closely with cholesterol to form nanodomains and function accordingly, thus providing a structural test of sphingolipid behavior in live cells.

Our results define a structural motif in the ceramide acyl chain of the GSLs that dictates endosomal sorting and with broad implications for current models of membrane structure and function.

RESULTS

The 11 GM1 molecules synthesized for testing contained saturated and mono-unsaturated acyl chains (Figure 1B) produced naturally in mammalian cells (Kavaliauskiene et al., 2014). Three additional molecules, the GM1 C12:1$^{\Delta 6}$, C12:0, and C16:1$^{\Delta 9}$ species, were prepared to contain non-native ceramide acyl chains that broadened the testing of the hypothesis (Figures 1B and S1A). The cellular and membrane behaviors of each GM1 species were studied by coupling the extracellular oligosaccharide to a "reporter" peptide containing biotin and fluorophore (Figures S1A and S1B) or directly to a fluorophore (Chinnapen et al., 2012; Garcia-Castillo et al., 2018; te Welscher et al., 2014). GM1 species were added to cells at nanomolar concentrations, resulting in PM incorporation at a fraction of naturally occurring GM1 (Figure S1C). Thus far, in all of our studies, the modified GM1 tracers behave like native GM1 (Arumugam et al., 2021; Chinnapen et al., 2012).

As a first test of membrane behavior, the liquid ordered (L_o) and liquid disordered (L_d) phase preferences for each of the GM1 species were defined *in vitro* using giant PM vesicles (GPMVs) prepared from different cell lines as indicated (Figures S1D–S1F). Certain saturated lipids and sterols can condense into higher ordered assemblies within biologic membranes, called the L_o phase. This separates them from the other lipids present in the same membrane called the L_d phase. Phase partitioning into the L_o phase can be considered a feature of nanodomains in live cells (Sezgin et al., 2012; Veatch, 2003). We found the major determinant for the phase behaviors of the different GM1 species in GMPVs to be the presence or absence of a *cis*-double bond in the ceramide acyl chain. The unsaturated GM1

species segregated into the L_d phase irrespective of the cell-type-specific GMPV tested. GM1 with fully saturated ceramide acyl chains associated exclusively with the L_o phase. Thus, partitioning into the L_o phase in GPMVs depended on full saturation of the fatty acyl chain.

A saturated acyl chain length of at least 14 carbon atoms in the GM1 ceramide directs sorting to the lysosome

We next used lattice light-sheet and airyscan microscopy to image the different fluorescently labeled GM1 species in the sorting endosome (SE) and their ability to enter endosomal sorting tubules. Endosomal sorting tubules affect the trafficking of membrane and cargo away from the lysosome and into the recycling pathway for return to the PM or into the retrograde pathway for transport to Golgi and endoplasmic reticulum (ER) (schematic, Figure 1A). For these studies, human A431 epithelial cells were co-incubated with nanomolar concentrations of the different GM1 species together with transferrin (Tfn) and dextran. Tfn and dextran were used to mark the endosome recycling and the lysosome pathways, respectively (Maxfield and McGraw, 2004; Mukherjee et al., 1997). SEs, which serve all pathways, were operationally defined as Tfn and dextran double-positive vesicles, and sorting tubules emerging from these structures were identified by their Tfn-only content. We tested several cell lines for this assay. The A431 cell line selected for these studies exhibited highly elongated and easily visualized tubules emerging from the SE. The same basic phenotypes, however, were observed in other A431 clones and HeLa (Figures S2A and S2B), MDCK II, Caco2, and HT29 cell lines, all of which lacked the unusually elongated tubules (data not shown).

We found that the GM1 species with ceramides containing short saturated acyl chains (≤C14:0) or unsaturated acyl chains C12:$1^{\Delta 6}$ through C22:$1^{\Delta 13}$ efficiently co-localized with Tfn in endosome sorting tubules (Figure 1C, left panels and quantified in Figure 1E and Video S1). The GM1 species with ceramides containing long saturated acyl chains ≥C16:0, however, did not (Figures 1C, right panels, and 1E; Videos S1 and S2). They were localized only to the body of the SE. We tested this observation again using the C18:0 and C18:1 ceramide pair loaded together into the same cells and obtained the same results (Figures 1D and 1F; Video S2).

Notably, we also found that the GM1 species containing ceramides with unsaturated but very long acyl chains (≥C24:$1^{\Delta 15}$ in length) were localized only in the body of the SE, behaving like the GM1 species with fully saturated acyl chains. These GSLs did not enter the narrow highly curved sorting tubules despite the presence of a *cis*-double bond in their ceramide acyl chain (Figures 1B and 1C, lower right panels, and 1E). In addition, the GM1 species with C14:0 or C22:$1^{\Delta 13}$ fatty acids displayed intermediate and closely similar phenotypes. They still entered endosome sorting tubules but less efficiently (measured as lower fluorescence intensity in recycling endosomal tubules) (Figures 1G and left panel of 1H). This observation was not explained by reduced endocytic uptake of the lipids (Figure 1H, right panel). Closely similar phenotypes for all of the GM1 species tested were found in HeLa cells (Figures S2A and S2B) and for the other epithelial cell lines noted above (data not shown). Thus, while the presence or absence of a *cis*-double bond in the ceramide

acyl chain dictated L_o and L_d phase partitioning in GPMVs, the position of the double bond within the acyl chain acted as the decisive factor for endosomal sorting in live cells. Lipid shape, on its own, was not sufficient to explain the differential sorting observed. These results, especially considering the intermediate behaviors of the C14:0 and C22:$1^{\Delta 13}$ ceramide species, showed that a saturated acyl chain length of at least 14 carbon atoms plus one forming either a saturated or unsaturated bond, extending from the C1 amide bond at the water-bilayer interface, was necessary for retention of GM1 in the body of the endosome. We henceforth call this structure the C14* motif (Figure 1I).

Independence from lectin binding

The C14* motif may be necessary but insufficient to explain the differential endosomal sorting of GM1 as endogenous lectins capable of scaffolding the lipid may be involved (Lakshminarayan et al., 2014). Such an effect on GM1 trafficking is perhaps best typified by multivalent binding to the β subunit of cholera toxin (CTxB) (Chinnapen et al., 2012; Kabbani et al., 2020; Kellie et al., 1983; Römer et al., 2007; Sorre et al., 2009). As such, we tested whether binding CTxB may act on the different GM1 species to affect changes in their L_d and L_o phase behaviors as assessed in GPMVs. The addition of CTxB caused a switch from L_d to L_o phase preference, but only for the GM1 species with very long unsaturated acyl chains ≥22:$1^{\Delta 13}$ (Figure S2C). The phase preferences for the other GM1 species were not affected.

To test in live cells whether cross-linking GM1 by endogenous lectins may be required for its endosomal sorting, we studied the GM1 C16:0 and C16:$1^{\Delta 9}$ pair and GM1 C24:$1^{\Delta 15}$. Here, intracellular trafficking of the different GM1 species was quantified in A431 cells continuously exposed to 100 mM lactose or sucrose to compete against binding the GM1 oligosaccharide moiety by endogenous lectins (Stillman et al., 2006). We found no effect of the disaccharide treatments (Figure S2E). Control studies showed that 100 mM lactose was sufficient to block the high-affinity binding of CTxB to GM1 on the A431 cell surface (Figure S2D). Thus, binding by endogenous galactose- or glucose-binding lectins does not appear to be required for the observed GM1 endosomal sorting (Figure 1C)—in these cases, the C14* motif is both necessary and sufficient.

Differential sorting between the lysosomal and recycling pathways

To quantitatively test whether endosomal GM1 sorting is based on the C14* motif, we developed a fluorescence-activated cell sorting (FACS)-based assay to measure GM1 sorting between recycling endosomes and lysosomes (Figure 1A, pathways A versus C). For these studies, we synthesized the GM1 library coupled to the all-D amino acid “reporter” peptide containing only a biotin functional group (Figure S1A). Conditions for incorporating the different GM1 species into the PM at similar amounts were determined experimentally (Figure 2A, left panel). After a 3-h “chase” time course, the amount of the biotin-labeled GM1 located at the cell surface was determined by FACS measured by binding of fluorescently labeled streptavidin (Figures 2A, 2B, and S3A). Early time course studies using GM1 C18:0 and GM1 C18:1Δ9 validated the FACS assay (Figure S3A). Here, we found that the surface staining for GM1 C18:1 Δ9 was initially diminished at the 30-min chase time point and returned to a steady-state level close to baseline after a 1-h chase. This

is consistent with endocytosis and recycling. In contrast, the cell surface staining for GM1 C18:0 decreased steadily over time, which is consistent with endocytosis and trafficking to the lysosome (Figure S3A). We found that the GM1 species that entered endosome sorting tubules and lacked the C14* motif (GM1 C12:0, C14:0, C16:$1^{\Delta 9}$, C18:$1^{\Delta 9}$, and C22:$1^{\Delta 13}$; Figures 1E, 2A, and 2B, magenta points) were recycled after endocytosis. They were detected on the PM at significantly higher levels compared to the GM1 species containing the C14* motif (GM1 C16:0, C18:0, C24:$1^{\Delta 15}$, C24:0, and C26:$1^{\Delta 17}$; Figures 2A and 2B, turquoise points). Even after longer chase times (>6 h), the GM1 C16:$1^{\Delta 9}$ species still localized to the PM and within endosomal recycling tubules containing Tfn, while the GM1 C16:0 species localized strictly to intracellular vesicles stained by lysotracker (marking late endosomes [LEs] and lysosomes; Figure S3B). We observed no confounding effects of GM1 treatment on endocytosis per se, as measured by dextran (fluid-phase) or Tfn (receptor-mediated) uptake (Figure S3D). In addition, the results could not be simply explained by differential endocytic uptake mechanisms into caveolae, as neither the C18:$1^{\Delta 9}$ nor C18:0 species were sensitive to the CRISPR-Cas9 deletion of cavin1 (Figure S3C). Thus, a saturated acyl chain length of at least 14 saturated carbon atoms plus one (the C14* motif) drives endosomal sorting of GM1 to the lysosome, with GM1 C14:0 and C22:$1^{\Delta 13}$ displaying intermediate phenotypes (Figures 1A, pathway 1C, and 2C). We note again that lysosomal sorting was rescued for the unsaturated GM1 species containing very long unsaturated acyl chains (i.e., unsaturated kinked-shaped fatty acids containing the C14* motif).

Cholesterol dependence for sorting to the lysosome

The nanodomain (lipid raft) hypothesis posits strong dependence on close assembly between GSLs and membrane cholesterol. We reasoned, however, that such cholesterol dependence should be evident for endosomal sorting of only the GM1 species with ceramide structures containing the C14* motif, if the motif acts as we hypothesize by allowing close alignment against the rigid and flat surface of cholesterol (London, 2005; Ramstedt and Slotte, 1999, 2002). Likewise, endosomal sorting of the GM1 species with *cis*-double bonds at positions disrupting the C14* motif should behave independently of membrane cholesterol. However, the GM1 species with a *cis*-double bond located beyond the C14* motif, as seen in the naturally occurring very long acyl chains (>C22:$1^{\Delta 13}$ acyl chains), should again show cholesterol dependence.

To test this idea, we studied the endosome recycling of the different GM1 species in A431 cells mildly reduced of membrane cholesterol either by treatment with low doses of the small-molecule inhibitors of cholesterol metabolism simvastatin, T0901317 or U18666A, or as we found experimentally by CRISPR-Cas9 knockout (KO) of serine-palmitoyltransferase-2 (SPTLC-2), ceramide synthase 5 (CerS5), or CerS2, or by simply growing the cells in over-confluent conditions. In all of the cases, the experimental conditions were found to lower PM cholesterol content as measured by loss of filipin staining (Figure S3F, left panel), and further evidenced by decrease in the general polarization (GP) of laurdan as assessed in GPMVs (implicating increased membrane fluidity typifying cholesterol-depleted membranes; Figure S3F, right panel). We also conducted lipidomic profiling by mass spectrometry, which showed in all of the cases that

cells were depleted of cholesterol and had only minor changes in the different species of the major membrane lipid classes: phosphatidylethanolamine (PE), phosphatidylglycerol (PG), and phosphatidylcholine (PC) (Figure S4D). In addition, and in all cases, cells depleted in cholesterol by our methods retained their normal endosomal and overall morphologies and endocytic uptake rates with only minor variations (Figures 2E, left panel, and S3E, compare simvastatin and T0901317 treatment to methyl-β-cyclodextrin [MβCD] treatment). We also note that cholesterol depletion induced by over-confluent cell culture, the least invasive perturbation, had only minimal effects on the overall lipidome and no detectable changes on phase preferences for any of the different GM1 species in GPMVs (Figure S3I).

Consistently, for all of the methods, we found no effect of cholesterol depletion on the recycling of GM1 species lacking the C14* motif (Figures 2D, magenta points, and S3G, left table). In contrast, cholesterol depletion uniformly affected the LE/lysosome sorting of GM1 species with ceramide moieties containing the C14* motif. This included the saturated acyl chains ≥C16:0 and notably the unsaturated ceramides with very long unsaturated acyl chains ≥C24:$1^{\Delta 15}$. In cholesterol-depleted cells, these GM1 species were no longer strictly sorted into the LE/lysosome; instead, large fractions of these lipids were recycled to the PM (Figures 2D, turquoise points, and S3G, right table) and co-localized within Tfn-containing endosome recycling tubules, where none was found before (Figures 2F and 2G). The effect of cholesterol depletion on lysosomal sorting was specific for GM1, as lysosomal sorting for the epidermal growth factor (EGF) receptor or the low-density lipoprotein receptor (LDLR) were not affected (Figures 2E, right panel, and S3H). Thus, the sorting step for trafficking GM1 into the lysosome appears to be dependent on membrane cholesterol, but only for the GM1 species with ceramide structures containing the C14* motif and predicted to interface tightly alongside the sterol, consistent with the nanodomain hypothesis.

Sorting into retrograde and recycling pathways by bulk membrane flow

We next considered the possibility that the GM1 species lacking the C14* motif may enter endosome sorting tubules by default, following bulk membrane flow (Mayor et al., 1993). If this were the case, we reasoned that these GM1 species should enter all of the pathways emerging from the SE, including the retrograde pathway to the *trans* Golgi and ER. For these studies, we used CTxB. Although CTxB scaffolds GM1 into a multimeric complex affecting its membrane behavior (Kabbani et al., 2020; Raghunathan et al., 2016; Wolf et al., 2008), ceramide structure still plays a decisive role in endosomal sorting into the ER (Chinnapen et al., 2012) and in liquid phase partitioning in GPMVs (Figure S2C). For these studies, the different GM1 species were applied to a HeLa cell line that endogenously lacks GM1. CTxB trafficking into the ER was quantitatively measured using a FACS-based split-GFP assay recently developed by our group (Luong et al., 2020). We found that only the short-chain (≤C14:0) or unsaturated GM1 species (≤C22:$1^{\Delta 13}$), both lacking the C14* motif, efficiently trafficked CTxB into the ER (Figures 3A and 3B). The GM1 species containing the C14* motif did not. This includes the GM1 species with ceramide structures containing long saturated acyl chains (≥C16:0) and those containing unsaturated but very long acyl chains (≥C24:$1^{\Delta 15}$), which rescue the C14* motif and its function. Thus, the requirement for acyl chain structure directing the different GM1 species into the retrograde endosomal pathway phenocopied exactly the structures required for sorting into the recycling pathway.

To confirm these results, we took an orthogonal approach and generated A431 cells containing CRISPR-Cas9 deletion of CerS2, the ceramide synthase producing very long acyl chain ceramides (>C20), or deletion of CerS5, the synthase producing ceramides containing short acyl chain ceramides (≤C16) (Park et al., 2014). These deletions genetically bias the structures of the endogenous GM1 ceramide moieties in CerS2 and CerS5 KO cells as just described. The approach was validated by lipidomic profiling of SM. SM and GSLs share the same ceramide biosynthetic pathway, and the abundance of SM in cell membranes allowed for the most conclusive analysis of endogenous ceramide structures. In wild-type (WT) A431 cells, the major SM species contained C18:0 (45%), followed by C24:1 (15–18%) and C18:1 (10%) acyl chains (Figure S4C). SM-containing ceramides with short acyl chains ≤C16 (6%–8%) were also reproducibly detected (n = 8 replicates). As expected in cells lacking CerS2, the SM species most strongly depleted were ceramides containing the very long acyl chains, but with the concomitant increase in C18:0 and C18:1, while in cells lacking CerS5, the SM species most strongly depleted were the short acyl chains ≤C16 and, unexpectedly, the C18 acyl chain species, with increases in C22:0 and C24:1.

When tested for GM1-dependent trafficking of CTxB, we found that the retrograde pathway was significantly reduced in those cells lacking CerS5 (Figure 3C), consistent with (1) the loss of the short and C18:1 acyl chain ceramides that lack the C14* motif and (2) the increased expression of the very long chain saturated ceramide species C22:0, including notably again those with an unsaturated bond positioned more deeply in the membrane (GM1 C24:$1^{\Delta 15}$). These ceramides contain the C14* motif. We found a slight increase in retrograde trafficking for cells depleted in Cer2, consistent with the depletion of only the very long chain ceramides and the modest increase in ceramides with C18:$1^{\Delta 9}$ (Figures 3C and S4C). Again, control studies showed that endocytosis and EGF/LDLR trafficking to the lysosome in CerS5 and CerS2 KO cells were not altered or slightly enhanced (Figures 2E and S3H).

Opposite results were found for sorting CTxB to the acidic lysosome as predicted. This was measured by FACS using CTxB coupled to the pH-sensitive fluorophore pHrodo. We found that CTxB-pHrodo fluorescence was reduced in the A431 cells deleted in CerS2, consistent with the loss of very long acyl chain ceramides containing the C14* motif and increase in the unsaturated C18:$1^{\Delta 9}$ ceramide lacking the motif (Figure 3D). For cells deleted in CerS5, which expressed higher levels of very long acyl chain ceramides (C20:0, C22:0, and C24:$1^{\Delta 15}$), we found a slight increase in lysosomal transport, consistent with the enhanced expression of GM1 lipids containing the C14* motif. Thus, the genetically modified cell lines phenocopied the trafficking of GM1 observed using exogenously applied and structurally defined GM1 species.

Cholesterol depletion had the same effect (Figure 3E). Here, we also observed an increase in retrograde trafficking to the ER (Figure 3F). These results implicate a selective and cholesterol-dependent process for retention within the body of the endosome followed by maturation to lysosomes for the GM1 ceramides that contain the C14* motif (Figures 3E and 3F). GM1 species lacking the C14* motif escape this lysosomal sorting step and sort, perhaps passively by following bulk membrane flow, into endosome tubules serving the recycling and retrograde endocytic pathways.

The C14* motif drives nanodomain assembly and segregation at the PM

The cholesterol dependency observed for C14* motif-based GM1 sorting to the lysosome is consistent with the idea that the mechanism of such sorting may involve assembly into membrane nanodomains. To test this, we imaged the GM1 C18:0 and C18:$1^{\Delta 9}$ species in SEs artificially enlarged to enable visualization by the overexpression of dominant active Rab5Q79L (tagged with EGFP). We found clear separation of the two GM1 species in the plane of the endosomal membrane (Figures 4A and 4B) and clear segregation between GM1 C18:0 (but not GM1 C18:$1^{\Delta 9}$) and the Tfn-Tfn-R complex. Again, the unsaturated very long acyl chain GM1 C24:$1^{\Delta 15}$, which also contains the C14* motif, was found to behave like GM1 C18:0. These results imply nanodomain formation within the SE. Notably, the clear segregation of the two unsaturated GM1 species C24:$1^{\Delta 15}$ and C18:$1^{\Delta 9}$ into distinct endosomal nanodomains in live cells was not predicted by their phase behaviors in GPMVs (Figures S1D–S1F). In those studies, phase separation was dictated by the presence or absence of *cis*-double bond (kinked or straight shapes). In live cells, as evidenced here, we find the C14* motif to be the decisive factor, not lipid shape.

We were then curious to know whether such segregation by nanodomain formation may also occur in the PM, before the lipids were internalized by endocytosis. To test this, we measured the diffusion rate of GM1 C18:0, C18:$1^{\Delta 9}$, and C24:$1^{\Delta 15}$ in PMs of A431 cells using fluorescence recovery after photobleaching (FRAP). We found slower rates of FRAP for the GM1 C18:0 and C24:$1^{\Delta 15}$ species (which contain the C14* motif) compared to GM1 C18:$1^{\Delta 9}$ species (which lacks the C14* motif) (Figure 4C). Thus, even in the PM, the distinct behaviors among the different GM1 species appears to be dictated by the C14* motif. The slower diffusion of the GM1 C18:0 and C24:$1^{\Delta 15}$ species is consistent with their assembly in membrane nanodomains linked to the subcortical cytoskeleton (Spillane et al., 2014).

To test whether these differences in PM mobility correlated with differences in uptake, we measured the apparent rate of endocytosis. Here, we used SVGA cells endogenously expressing Rab5-GFP to measure the co-localization between the different GM1 species and Rab5 early endosomes. Uniformly, after short 5- to 10-min incubations, little co-localization with Rab5 endosomes was observed for GM1 ceramides containing fully saturated C16:0, C18:0, and C24:0 acyl chains and for the very long unsaturated acyl chain GM1 C24:$1^{\Delta 15}$ (Figure 4D). These ceramides contain the C14* motif. The result implicates slow rates of endocytosis or very fast transition to Rab 7 LEs (or both) for these GM1 species. In contrast, we found a much higher degree of co-localization between the Rab5 endosome and GM1 ceramides containing the C16:$1^{\Delta 9}$ and C18:$1^{\Delta 9}$ acyl chains, which lack the C14* motif, consistent with rapid rates of endocytosis or efficient recycling (or both). The same results were obtained using Tfn, which we used as a control, phenocopying the C16:$1^{\Delta 9}$ and C18:$1^{\Delta 9}$ GM1 species (Figure 4D).

When the SVGA cells were depleted of cholesterol, however, co-localizations of the GM1 C16:0 and very long C24:$1^{\Delta 15}$ acyl chain species with Rab5 endosomes were increased (Figure 4E). These lipids also displayed an increase in their PM mobility after cholesterol depletion as assessed by FRAP (Figure 4F, compare black with magenta lines, and Figure S5A for quantification). When the SVGA cells were supplemented with additional

exogenous cholesterol, the degree of co-localization with Rab5 endosomes was diminished for the same GM1 C16:0 and C18:0 species and for the very long unsaturated acyl chain C24:$1^{\Delta 15}$ species compared to control untreated cells (Figures 4G and S5B). This phenotype induced by cholesterol addition was more readily apparent in HT29 and A431 cells, where PM localization was prominently marked at cell-cell contact sites. Here, these lipids appeared to be visibly "trapped" on the PM after cholesterol addition (Figures 4G, 4H, and S5D). Notably, the addition of cholesterol to SVGA cells had no detectable effect on the apparent efficiency of co-localization with Rab5 endosomes for the unsaturated GM1 species C16:$1^{\Delta 9}$ and C18:$1^{\Delta 9}$ (all lacking the C14* motif) or for Tfn used as control. We found no confounding effect of cholesterol treatment on fluid-phase dextran endocytic uptake or EGFR/LDLR sorting to the lysosome (Figure S5F).

Further evidence that excess membrane cholesterol caused the retention of GM1 species containing the C14* motif on the PM was obtained in A431 cells as assessed by FACS (Figure S5E) and by confocal microscopy (Figure 4H), and with no evidence for co-localization within Tfn^{+} endosome recycling tubules (Figure S5D). We also found a striking reduction in PM diffusion rates for the C18:0 and C24:$1^{\Delta 15}$ species in A431 cells treated with exogenous cholesterol, as assessed by FRAP (Figures 4I and S5A and see Goodwin et al., 2005). These results suggest nanodomain assembly for the C16:0, C18:0, and notably C24:$1^{\Delta 15}$ GM1 lipids, all of which contain the C14* motif.

Thus, overall, we found that the different GM1 species are sorted within live cells based on the C14* motif. These GM1 species were retained within the body of the SE for maturation along the lysosomal pathway (Figure 1A, pathway C). They exhibited dependence on membrane cholesterol for their sorting and biophysical behaviors, consistent with an affinity for assembly into membrane nanodomains (Figure 5). In contrast, the GM1 species containing mono-unsaturated acyl chains of 12–22 hydrocarbons atoms in length (thus lacking the C14* motif) did not display dependence on cholesterol for their membrane behaviors. Unlike the fully saturated GM1 species, these GSLs entered endosome sorting tubules of the recycling and retrograde endosome pathways.

DISCUSSION

The results of our studies show that mammalian cells sort GM1 sphingolipids between endosomes and endosome sorting tubules, and within the plane of the PM, based on their ceramide acyl chain structure. This is explained by differential association with membrane cholesterol, likely mediated by lipid nanodomain formation (Figure 2C and schematic in Figure 5). Lipid shape on its own (Baumgart et al., 2003; Mukherjee et al., 1999; Roux et al., 2005; Sorre et al., 2009) cannot fully explain the selective entry of the different GM1 species into the narrow highly curved endosome sorting tubules or their retention in the body of the SE. The differential sorting phenotypes observed were strictly dependent on membrane cholesterol content and ceramide structure, and the same structure-function relationships operated across multiple cell types known to vary in their overall membrane thickness, fluidity, and cholesterol content (data not shown and Hao et al., 2004; Noutsi et al., 2016; Steinkühler et al., 2019). These results define a structural organizing principle for complex sphingolipid behavior in native heterogeneous and dynamic live cell membranes.

The complex sphingolipids critically require more than 14 saturated hydrocarbons in the ceramide acyl chain extending from the C1 amide at the water-bilayer interface for optimal association with cholesterol. This decisively affects their direction of endosome sorting. GSL species lacking these features escape the apparently active lysosomal sorting step and enter endosome sorting tubules of the recycling and retrograde pathways instead. These observations experimentally verify in live cells one of the underlying and fundamental biophysical processes hypothesized to shape lipid trafficking, membrane architecture, and cell function. It is possible that the C14* motif may also explain the differential sorting of ceramide-linked proteins in the secretory pathway recently observed in yeast (Rodriguez-Gallardo et al., 2020).

In nature, the *cis*-double bond in the GM1 species containing mono-unsaturated acyl chains of 16–22 hydrocarbons atoms in length is positioned at carbon atom 9 or 13 (Δ^9 and Δ^{13}) extending from the amide linkage to sphingosine, and thus located within the outer leaflet of the membrane bilayer. Within this area, the kink in the acyl chain caused by unsaturation interferes with alignment against the flat and rigid sterol structure of cholesterol (Fanani and Maggio, 2017a, 2017b; Jaikishan et al., 2010; Kihara, 2012; Ramstedt and Slotte, 1999; Stockton and Smith, 1976). These GM1 species entered endosome sorting tubules of the recycling and retrograde endosome pathways, and their trafficking was not dependent of cholesterol. However, the GM1 species containing the very long mono-unsaturated acyl chains (C24:1$^{\Delta 15}$ and C26:1$^{\Delta 17}$) trafficked to the lysosome, phenocopying the fully saturated GM1 species even though they also contained a *cis*-double bond kink in their ceramide. Here, the structural analysis was most informative. The *cis*-double bond in these native acyl chains is located at Δ^{15} or Δ^{17}, below the stretch of 14 saturated hydrocarbons from the amide linkage at the membrane surface (Kihara, 2012), and below the expected interface with the sterol rings of cholesterol (Ramstedt and Slotte, 1999). Thus, the acyl chains of these GM1 species recapitulated exactly the minimal saturated hydrocarbon chain length that we found required for endosome sorting of the GSLs to the lysosome. Notably, the membrane behavior of these very long unsaturated GM1 species in live cells was strictly dependent on membrane cholesterol, analogous to the fully saturated acyl chain GM1 species. Two species GM1 C14:0 and GM1 C22:1$^{\Delta 13}$ had intermediate phenotypes for cholesterol dependence; these ceramides have acyl chain lengths that border on the minimal C14* motif required for functional association with cholesterol.

The strong dependence on cholesterol for the membrane behaviors of the saturated and very-long-chain unsaturated GM1 species conforms to central tenants of the lipid raft hypothesis. The raft hypothesis posits that certain lipids and cholesterol phase separate into ordered and tightly packed domains, mediated through hydrogen bonding and van der Waals forces, and shaped by cellular protein scaffolds, including by bonding to the cortical actin cytoskeleton (Sezgin et al., 2017; Simons and van Meer, 1988; Simons and Vaz, 2004). For the saturated and very-long-chain unsaturated GSLs, we find evidence for their assembly into membrane nanodomains, perhaps best evidenced by the segregation of these GM1 species in separate regions of artificially enlarged early endosomes. Our results are consistent with another structural factor implicated in nanodomain assembly for GPI-anchored proteins and recently for GM1 (Arumugam et al., 2021; Raghupathy et al., 2015): the need for direct extension of outer-membrane lipids into the inner-membrane lipid leaflet for assembly with

phosphatidylserine and the cortical actin cytoskeleton. In those studies (Arumugam et al., 2021), we found that the ceramide C14* motif was required for features of nanodomains with linkage to the cortical cytoskeleton as assessed by fluorescence correlation microscopy. Nanodomain formation and GM1 trafficking may also be affected by extracellular factors that induce lipid clustering (Johannes et al., 2015), as we found for CTxB (Chinnapen et al., 2012).

The structural diversity of ceramide moieties comprising the complex sphingolipids that occur in nature is perhaps best defined for SM, which is the most highly prevalent complex sphingolipid, and thus most easily and reproducibly studied. In our hands, and in the cell type examined, we found that the predominant ceramide moieties in SM contained C18:0, C18:1$^{\Delta 9}$, C24:0, and C24:1$^{\Delta 15}$ acyl chains. This and published lipidomic analyses of SM in other cell types suggest the evolution of two “bimodal” structure-function distributions for the complex sphingolipids: one between long and very long ceramide acyl chains, as proposed before (61–64; Shaner et al., 2009), and the other between saturation and unsaturation as we find here. Experimentally, these two bimodal distributions were evident in our structure-function studies on GM1. In the case of unsaturation, the different membrane behaviors were most readily apparent for the saturated GM1 C18:0 and the unsaturated C18:1 species, but this dichotomy of saturation and unsaturation was not absolute—it also depended on acyl chain length. In the case of GM1 species with very long C24:0, and C24:1$^{\Delta 15}$ acyl chains, for example, these GSLs behaved mostly in the same way, even though one was saturated and the other was not. Thus, acyl chain length in the native complex sphingolipids appears to override the functional impact of unsaturation, as long as the *cis*-double bond is positioned below a stretch of saturated hydrocarbons of sufficient length (beyond the C14* motif). The long and very long acyl chains may also enable interdigitation with the contralateral lipid leaflet (Fujimoto and Parmryd, 2017; Róg et al., 2016; Skotland and Sandvig, 2019). Lipid shape, on its own, does not appear to act decisively for entry of the GSLs into endosome sorting tubules, or for their endosomal sorting in live cells, contrary to the impact of acyl chain unsaturation on L_d and L_o phase separation and nanodomain assembly in GPMVs *in vitro*.

We also note that some very long unsaturated acyl chain GM1 species, typified by GM1 C24:1$^{\Delta 15}$, exhibited graded membrane behaviors that bridged the dichotomy between saturation and unsaturation seen in the GM1 C18:0 and C18:1 pair. These very long acyl chain GSLs sorted predominantly to the lysosome, but a significant portion sorted also into the recycling pathway, in contrast to their fully saturated counterparts. In addition, GM1 C24:1$^{\Delta 15}$ had a restricted but still higher degree of apparent endocytic uptake compared to its fully saturated counterpart. Thus, the very-long-chain unsaturated GSLs appear to occupy a functionally intermediate space. They may have been evolutionarily conserved according to their graded membrane behaviors in membrane sorting so as to more readily enable differential responses to small alterations in membrane structure and composition caused by cell stress, cell differentiation, or even to the normal dynamic changes in membrane content produced by trafficking from one organelle to another in cells at steady state (Nyholm et al., 2019).

In summary, our studies show that the membrane behaviors of the complex sphingolipids are defined by two general rules of ceramide structure, hydrocarbon acyl chain length and unsaturation. This includes the position of the *cis*-double bond with respect to the outer leaflet of the membrane lipid bilayer and how acyl chain length and saturation affect the ability of GSLs to associate with cholesterol and possibly to form nanodomains. These basic structural principles are of general importance to cell and tissue biology, as the segregation and behavior of lipids have fundamental physiological consequences for membrane organization and the plasticity required to accommodate the diversity of membrane dynamics underlying cell functions.

STAR★METHODS

RESOURCE AVAILABILITY

Lead contact—Further information and requests for resources and reagents should be directed to and will be fulfilled by the lead contact, Wayne Lencer (wayne.lencer@childrens.harvard.edu).

Materials availability—Plasmids and cell lines generated in this study will be made available upon request.

Data and code availability

- All unique reagents generated in this study, further information regarding the synthesized of GM1 species and lipidomic profiling data are available from the lead contact upon request.
- This paper does not report original code.
- Any additional information required to reanalyze the data reported in this work paper is available from the lead contact upon request.

EXPERIMENTAL MODEL AND SUBJECT DETAILS

Cell lines—Human epithelial A431, HT29, CaCo and Hela cells, as well as HEK293T cells were originally purchased from the American Tissue Culture Collection (ATCC, VA).

METHOD DETAILS

Cell culture—Cells were maintained in Dulbecco's modified Eagle's medium (DMEM) containing 10% FBS with penicillin and streptomycin. Cultures were split two days prior to experiment to achieve the desired confluency state. The CRISPR-Cas9 SVGA Rab5-GFP cell line was maintained in MEM containing 10% FBS (Chou et al., 2016).

For cholesterol addition and/or depletion assays, cells were cultured for 24 h in [50–100 nM] T0901317, or for 12 h in [1–2 μg/mL] U18666A in full medium and for 24 h for [10 μM] simvastatin in serum depleted of HDL. Soluble cholesterol complexed to MβCD [120 μg/mL] was given in full media for 30 min or the indicated time. Efficacy of treatment was determined by fixing treated cells in 4% paraformaldehyde for 1 h and subsequently staining cells with [0.05 mg/mL] filipin III to determine plasma membrane cholesterol contents by

fluorescence. Plasma membrane fluorescence intensity was measured using the Fiji (ImageJ, National Institutes of Health, Bethesda, MD, USA) segmented line tool to outline plasma membrane and mean grey values were obtained.

To obtain enlarged Rab5 early endosomes, A431 cells were transfected using Lipofectamine® 2000 and OptiMEM® transfection method according to manufacturer's instructions and 500–1000 ng of the Addgene plasmids (#28046, #35138).

Generation of CRISPR-Cas9 KO cell lines—CRISPR-Cas9 KO cell lines were generated using Addgene plasmid lentiCas9-Blast (#52962) for stable integration of Cas9 endonuclease and guide sequences were cloned into Addgene plasmid lentiGuide-Puro (#52963) against ceramide synthase 1, 2 and 5 (CerS1, 2 and 5), UDP-glucosyl-ceramide glucosyltransferase (UGCG), and serine palmitoyltransferase 2 (SPTLC-2) (CRISPR KO guides sequences were used from AVANA sgGuide library (Doench et al., 2016)).). Plasmids were verified by sequencing using IDT technologies (Coralville, IA). [1.5 μg] plasmids were co-transfected with packaging plasmids pVSVg [0.5 μg] and psPAX2 [1 μg] Addgene plasmids #8454, #12260 in the presence of polyethylenimine (PEI) into HEK293T cells for lentivirus production. 48 h post transfection virus was harvested and mixed with respective cell line. Clones were selected for 7 days on [10 μg/mL] Blasticidin and/or [1 μg/mL] Puromycin. KO cell lines were tested for CTxB binding by FACS and low binding population was sorted.

Cell lines carrying an ER version of Split-GFP were constructed according to Luong *et. al.* (Luong et al., 2020) and selected on Hygromycin [50 μg/mL] for 7 days.

Synthesis of peptide and fluorophore-labeled GM1 species—Gangliosides of various fatty acid species were supplied by Prof. Sandro Sonnino (U. Milan, Italy). Reporter peptide containing modified functional residues were custom synthesized by New England Peptide (Gardner, MA) as all-D peptides with the following amino acid sequence: propargylglycine-k(ε-biotinoyl)(ds)g(dy)g(dr)g(ds)g-(kaoa)-amine. Synthesis of peptide-lipid and fluorophore labeled conjugates was accomplished with minor modifications according to Garcia-Castillo et al., te Welscher et al. and Chinnapen et al. (Chinnapen et al., 2012; Garcia-Castillo et al., 2018; te Welscher et al., 2014).

In a typical 2 mL reaction, 2 mg (approximately 1300 nmoles) of ganglioside was oxidized with sodium periodate (13 mmoles) in oxidation buffer (100 mM sodium acetate pH 5.5, 150 mM NaCl) for 30 min on ice. The reaction was quenched by addition of glycerol (5% final) and desalted using a Bond Elut SepPak C18 cartridge (Agilent, MA). Methanol was used to elute oxidized GM1 species from the column and was removed by Speed Vac concentration (Savant). The oxidized product was then reconstituted in 2 mL PBS pH 6.9 in the presence of 10% DMF and reacted with 2700 nmoles of aminooxy-containing peptide in the presence of 10 mM aniline (Dirksen and Dawson, 2008). The reaction was incubated for 20 h at room temperature with mixing on a nutator. The precipitate was separated from the solution by centrifugation, and then resuspended in 400 μL 50% isopropanol/water after brief sonication. PBS pH 6.9 was added (200 μL) along with 4.8 mmoles of sodium cyanoborohydride and incubated for 3 h to reduce the oxime bond. Lipid-peptide

conjugates were purified by semi-preparative HPLC, and confirmed by either MALDI-TOF (AB Voyager), or ESI LC-MS (Agilent, MA).

Peptides were labeled with Alexa fluorophore via copper mediated Click chemistry. 320 mM peptide-lipid fusions containing an N-terminal alkyne residue (propargylglycine) were reacted with equimolar concentrations of AlexaFluor™ -azide under the following conditions: 50 mM Tris-Cl, 5 mM copper (II) sulfate, 100 mM sodium ascorbate, 37 mM (Tris[(1-benzyl-1H-1,2,3-triazol-4-yl)methyl] amine, TBTA in DMSO/t-butanol 1:4) 1 mM (Tris(2-carboxyethyl) phosphine hydrochloride, TCEP) for 16 h at room temperature on a nutator. Products were purified by HPLC and confirmed by mass spectrometry. Products were lyophilized and stored at − 20°C or − 80°C for long term storage. Traces can be accessed under https://doi.org/10.17632/bk7cmygrdr.1.

Working stock solutions were prepared in 33% DMF/ddH20—Alternatively, fatty acyl variant gangliosides were fluorophore labeled directly via the oligosaccharide head group following the oxidation of the ganglioside. The oxidized gangliosides were resuspended in phosphate buffered saline pH 7.4 (PBS) and reacted with 1 mole AlexaFluor™-azide (Invitrogen, OR) for 16 h. Ten moles sodium cyanoborohydride was added to the reaction for 15 min and the mixture was desalted on Bond-Elute cartridges. Ganglioside-fluorophore conjugates resulted in a different mobility band visible by TLC and were purified using preparative-TLC plates. Extraction from silica scrapings was performed, and the conjugates further purified by reversed phase C18 cartridges.

FACS based assay for lipid recycling, retrograde and lysosomal trafficking— Cell lines were plated on 96 well plates and grown to 70% confluency (unless otherwise stated) with or without treatment. Cells were washed and equilibrated with serum-free DMEM (no phenol red) for 5 min at 37°C. GM1 species were diluted to four different concentrations of the respective peptide-labeled GM1 species in serum-free DMEM with equimolar ratio of dfBSA (1:1 lipid:dfBSA). Lipids were loaded for 10 min at 37°C and washed of in serum-free DMEM (no phenol red). To measure the amount of ‘loaded’ GM1, cells were trypsinized for 5 min at 37°C, then chilled to 4°C and stained with respective streptavidin-AlexaFluor™ (1:2500, 2 mg/mL) in PBS containing 5% BSA for 15 min/4°C. Unbound streptavidin was washed off twice with PBS containing 5% FBS and cells were FACS analyzed immediately, using a FACS Canto II (BD, Biosciences, NJ). Lipid + gate was determined against streptavidin stained control cells, not loaded with GM1. The percentage of positive cells and their median fluorescence were recorded. To compare the recycling efficiency between the different GM1 variants, the respective concentrations resulting in equal median fluorescence or equal % of cells for the ‘load’ were chosen. To obtain ‘chase’ samples, the lipid was washed off and cells were subsequently incubated for 3 h in DMEM containing 5% FBS in the presence of Dextran-Fluor (500 μg/mL) and transferrin-AlexaFluor™ (1 μg/mL). Cells were then washed and trypsinized and stained with streptavidin-AlexaFluor™ as described above. To compare recycling rates between different treatments, recycling rates (median fluorescence) for non-treated or WT cells were normalized to 1 and fold change difference to treated samples calculated.

To determine retrograde trafficking of CTxB-SplitGFP, native (non-peptide labeled) GM1 species were loaded as above into either Hela cells or an A431 CRISPR-Cas9 UGCG-KO cell line, expressing the large bit of $mNG2_{1–10}$ fused to the signal sequence of BIP and the C-terminal ER-retention motif KDEL as described in Luong et al.. CTxB-SplitGFP was generated by fusing the N-terminus of the CTx A2-chain to the small bit peptide $mNG2_{11}$ and this construct was coexpressed in E. coli with CTxB. The assembled CTxB pentamers containing the A2 small bit peptide $mNG2_{11}$ were then purified as described in more detail in (Luong et al., 2020). The ‘load’ amount of lipid was determined using 5nM fluorescently labeled CTxB instead of streptavidin as described above. ‘Chase’ samples were incubated in the presence of 10 nM CTxB-SplitGFP for the indicated amount of time in DMEM containing 5% FBS. For retrograde trafficking in CRISPR-Cas9 KO cell lines, cell surface GM1 amount was determined using 5nM fluorescently labeled CTxB as described above and CTxB-SplitGFP values were normalized to cell surface GM1.

To measure lysosomal trafficking of GM1-CTxB complex, pH sensitive CTxB-pHrodo™ was used. Cells were chilled to 4°C and stained using 5 nM CTxB-pHrodo™ in PBS containing 5% BSA. Unbound CTxB was washed off and cells were incubated for the indicated amount of time at 37°C in in DMEM containing 5% FBS. Cell surface GM1 was determined using 5nM fluorescently labeled CTxB as described above and CTxB-pHrodo™ values were normalized to cell surface GM1.

Two biological replicates per assay were performed and a total of N = 10,000–20,000 single cells recorded per treatment for all FACS based assays.

Lysosomal trafficking of EGF receptor and LDL receptor—Cells were grown as described above. To determine the lysosomal fraction of different membrane protein receptors, cells were loaded with their respective ligands at (2–5 μg/mL), labeled either as pH sensitive (phrodo™, FITC) or pH resistant (AlexaFluor™/Bodipy for LDL). ‘Load’ was determined by incubating pre-chilled cells for 10 min at 4°C with pH resistant ligand. Cells were subsequent washed in PBS and detached using Cell Dissociation Buffer (Gibco). Lysosomal fraction was determined by loading cells with pH sensitive ligand as above; after washing off unbound ligand, cells were moved to 37°C for 2 h in the presence of fluorescent dextran to normalize endocytosis rates. Cells were trypsinized and subsequently analyzed by FACS.

Lipid loading, imaging and quantification for airyscan or lattice lightsheet imaging—Cell lines were plated on either 35 mm MatTek petri dishes (Ashland, MA) containing glass bottom for Airyscan confocal microscopy or on 3 mm cover slips for Lattice Lightsheet microscopy and grown to 70% confluency with or without treatment. Fluorescent GM1 variants were added as described for the FACS based assays for lipid recycling unless otherwise noted. To determine subcellular location, lipids were allowed to traffic for the indicated amount of time at 37°C in the presence of fluorescent transferrin (1 μg/mL) and lysoTracker™ (2 nM) or dextran (1 mg/mL) to demarcate the respective organelles. Sorting endosomes were defined as vesicles containing lipid as well as transferrin and dextran. Sorting endosomal tubules were defined by presence of transferrin emerging from triple positive vesicles.

For lactose and sucrose addition experiments A431 cells were incubated for 30 min in the presence of 100 mM lactose or sucrose prior/during and after GM1 loading.

Airyscan imaging was performed using Zeiss LSM 880 microscope with Airyscan detector and Plan-Apochromat 63x oil immersion objective with NA = 1.4. Airyscan processing was performed using the Zeiss ZenBlack software.

Quantification of GM1 in recycling endosomal tubules: Region of interest (ROI) was determined, containing approximately 3–6 triple positive vesicles and the ROI was thresholded using image quantification software ImageJ (Otsu). GM1 presence/absence (1/0) within transferrin positive tubules was recorded and % for the ROI calculated.

Tubule over vesicle fluorescence quantification: For GM1 C14:0 and C22:1$^{\Delta 13}$ as well as for samples treated with cholesterol lowering molecules, or cholesterol addition, fluorescence grey values for the vesicle and tubule were recorded, background fluorescence was subtracted and a ratio was determined by dividing the mean grey value obtained for the tubule by the mean grey value obtained for the vesicle (Figure 1H). The same analysis was performed for Figures 2G and S4D.

Quantification of endocytic uptake: Endocytic uptake was assayed using CRISPR-Cas9 modified SVGA cell line containing an endogenous, RAB5-EGFP variant (Chou et al., 2016). GM1 variants were loaded as described above, washed off and immediately transferred to the microscope. Cells were imaged for approx. 5 min each. Cell outlines were defined, images were thresholded and Mander's coefficients calculated using ImageJ software. M2 is displayed and signifies amount of Rab5-EGFP signal co-localizing with GM1 signal. Quantification was based on at least 5 biological replicates.

GM1 - Tfn co-localization in Rab5 enlarged early endosomes: Using Fiji segmented line tool Rab5 early endosomes were traced using Rab5 fluorescence as marker and mean grey fluorescence intensity profiles of GM1 variants and Tfn were exported into GraphPad Prism. Pearson's correlation coefficient was calculated between different GM1 or Rab5 fluorescence profiles against Tfn fluorescence profile.

Fluorescence recovery after bleaching (FRAP)—Cell lines were plated on 35 mm MatTek petri dishes containing glass bottom 48 h prior to experiments and treated as described above. GM1 lipids were incorporated into plasma membranes as described above.

Cells were immediately transferred into preheated chamber for bleaching using the following settings: 80–100% laser intensity, pixel dwell time of approx. 170 μsec, membrane fluorescence was bleached to about 20–40% of the original fluorescence intensity. Three ROIs of similar size were chosen, one background ROI (ROI_{bg}) and two ROIs within the PM of a given cells, with one of the latter being bleached (ROI_b), while the other served as reference photobleaching control (ROI_{nb}). To establish the baseline, three – five frames were collected before the bleaching event and to capture the recovery, at least fifteen frames were acquired every 150–300 msec for a total time of approx. 10 s post bleaching event.

FRAP curves were determined using the following formulas with pb = pre bleached fluorescence (Nissim-Rafinia and Meshorer, 2011):

1. $$Bleached\ Fraction(t) = 1 - \left[\frac{\left(ROI_{b(t)} - ROI_{bg}\right)}{\left(ROI_{nb(t)} - ROI_{bg}\right)} * \frac{\left(pbROI_{nb} - pbROI_{bg}\right)}{\left(pbROI_{b} - ROI_{bg}\right)}\right]$$

2. $$Fluorescence\ Recovery = Bleached\ Fraction(t_{max}) - Bleached\ Fraction(t_{right\ after\ bleach})$$

3. $$Mobile\ Fraction = \frac{Fluorescence\ Recovery}{Bleached\ Fraction\left(t_{right\ after\ bleach}\right)}$$

GPMV generation—Cells were seeded two days prior to assay on 12 well plates to reach desired confluency. Native or fluorescently labeled GM1 species were added as described above, and a phase marker (*FAST*DiO™ and *FAST*DiL™, 0.5 mg/mL − 1. 1:1000 in PBS) was added for 10 min. Phase marker was washed off three times using PBS, then cells were equilibrated by washing twice in GPMV buffer (50 mM Tris, pH = 8, 150 mM NaCl, 50 mM $CaCl_2$). Vesiculation was achieved according to (Sezgin et al., 2012) by using 2 mM DTT and 0.07% PFA in GPMV buffer and cells were incubated for 1–3 h at 37°C (depending on the cell type). Supernatant containing GPMV vesicles were harvested and sedimented 5 min/500 g. Vesicles were chilled to 10°C and imaged. L_d phase was determined by the phase marker and L_o partitioning coefficient (ordered phase partitioning coefficient = I_{lo}) was obtained using the following formula: $K_{raft} = I_{Lo}/I_{Ld}$. A $K_{lo} > 1$ indicates ordered phase preference.

For membrane fluidity analysis, GPMVs were harvested from respective cells and/or treatments as above and subsequently stained using [0.5 μM] laurdan for 3 h at RT. Dye was washed off twice and vesicles were chilled to 10°C prior to imaging. Imaging was achieved by using spectral imaging with confocal microscope Zeiss LSM 880 using Plan-Apochromat 63x oil immersion objective (NA 1.4). C-laurdan was excited at 405 nm and the emission was collected with a multichannel spectral detector (PMT) in the range 430–450 nm and 480–500 nm simultaneously. The polarity index, generalized polarization (GP) was calculated according to Steinkuehler et al. (Steinkühler et al., 2019) using the following formula: $GP = (I_{440} - I_{490})/(I_{440} + I_{490})$ where I_{440} and I_{490} are the fluorescence intensities at 440 nm and 490 nm, respectively.

Lipid extraction and lipidomic profiling of A431 WT and CRISPR-Cas9 KO cell lines—500,000 cells per biological/technical replicate were washed twice with PBS and then 0.25 × PBS to remove media components and transferred into glass vials. Cells were then pelleted to remove remaining supernatant and flash frozen in liquid nitrogen and pellet was subsequently lyophilized. Lipid extraction and lipidomic profiling was performed according to Liaw *et. al.* and Kumar *et. al.* (Gajenthra Kumar et al., 2018; Liaw et al., 2016). In brief, the lyophilized pellet was homogenized in 1 mL ddH_2O, subsequently 2.2 mL methanol and 0.9 mL dichlormethane was added. Suspension was incubated o/N at −20C, before 20 μL Avanti Splash mix was added, mixture was vortexed and incubated for 10 min at RT. Then 1 mL ddH_2O, 0.9 mL dichloromethane and 0.5 mL methanol were added. Solution was centrifuged at 1200 rpm for 10 min and lower phase collected into fresh glass

tube. 2 mL dichloromethane were added to the aqueous phase to extract any remaining lipids, mixture was centrifuged as above and the organic phase was pooled with the first one.

Solvent was evaporated in Genevac.

Unbiased MS/MSALL shotgun lipidomic profiling was performed on Sciex 5600 TripleTOF mass spectrometer.

QUANTIFICATION AND STATISTICAL ANALYSIS

Imaging data was analyzed using either Zeiss ZENblack, Fiji or Aiviva 9 (Drvision Technologies, Bellevue, WA) software. Lattice lightsheet data obtained at the Janelia Farms Advanced Imaging center (AIC), deskewed and decovoluted using customized Matlab™ software.

Schematic Model in Figure 1A was drawn using BioRender.

Mean grey fluorescent values of microscopy experiments or mean fluorescence data obtained from FACS experiments was transferred to GraphPad Prism software (San Diego, CA) for graphing and statistical analysis. Statistically significant difference between treatments was tested by One-way ANOVA with Tukey's multiple comparison; alternatively unpaired t-test was applied when indicated with n.s. $p > 0.05$, *$p < 0.05$, **$p < 0.01$ ***$p < 0.001$ and ****$p < 0.0001$.

Supplementary Material

Refer to Web version on PubMed Central for supplementary material.

ACKNOWLEDGMENTS

We thank the Janelia Farms Advanced Imaging Center for providing access and support for their Lattice Lightsheet microscope. Imaging data used in this publication was produced in collaboration with the Advanced Imaging Center, a facility jointly supported by the Gordon and Betty Moore Foundation and HHMI at HHMI's Janelia Research Campus. We further thank the Harvard Center for Biological Imaging, Boston Children's Hospital Cell Function and Imaging Core, and HDDC Imaging Core for infrastructure and support. We thank Prof. Dr. Kirchhausen (Boston Children's Hospital, Harvard Medical School) for providing the SVGA-Rab5-GFP cell line, as well as Prof. Dr. Waldor and Dr. Alline Pacheco (Brigham and Woman's Hospital, Harvard Medical School) for providing one CRISPR-Cas9 UGCG and SPTLC-2 KO plasmids and HT29 $Cas9^+$ cell line. We further thank Dr. Daniel Chinnapen, Dr. Richard Duclos, Dr. Phi Luong, and Dr. Jamie LeBarron for helpful discussions during the preparation of this manuscript and Profs. Thiagarajah (Boston Children's Hospital, Harvard Medical School), Johannes (Institut Curie), and Kenworthy (University of Virginia School of Medicine) for critically reading the manuscript. This work was supported by grants R37 DK048106 and RO1 DK104868 to W.I.L., and P30 DK034854 to the Harvard Digestive Disease Center.

REFERENCES

Arumugam S, Schmieder S, Pezeshkian W, Becken U, Wunder C, Chinnapen D, Ipsen JH, Kenworthy AK, Lencer W, Mayor S, and Johannes L (2021). Ceramide structure dictates glycosphingolipid nanodomain assembly and function. Nat. Commun 12, 3675. 10.1038/s41467-021-23961-9. [PubMed: 34135326]

Baumgart T, Hess ST, and Webb WW (2003). Imaging coexisting fluid domains in biomembrane models coupling curvature and line tension. Nature 425, 821–824. 10.1038/nature02013. [PubMed: 14574408]

Brown DA, and London E (1998). Structure and origin of ordered lipid domains in biological membranes. J. Membr. Biol 164, 103–114. 10.1007/s002329900397. [PubMed: 9662555]

Campanero-Rhodes MA, Smith A, Chai W, Sonnino S, Mauri L, Childs RA, Zhang Y, Ewers H, Helenius A, Imberty A, and Feizi T (2007). N-glycolyl GM1 ganglioside as a receptor for simian virus 40. J. Virol 81, 12846–12858. 10.1128/jvi.01311-07. [PubMed: 17855525]

Chiantia S, and London E (2013). Sphingolipids and membrane domains: recent advances. In Sphingolipids: Basic Science and Drug Development, Gulbins E and Petrache I, eds. (Springer Vienna), pp. 33–55.

Chinnapen DF, Hsieh WT, te Welscher YM, Saslowsky DE, Kaoutzani L, Brandsma E, D'Auria L, Park H, Wagner JS, Drake KR, et al. (2012). Lipid sorting by ceramide structure from plasma membrane to ER for the cholera toxin receptor ganglioside GM1. Dev. Cell 23, 573–586. 10.1016/j.devcel.2012.08.002. [PubMed: 22975326]

Chou YY, Cuevas C, Carocci M, Stubbs SH, Ma M, Cureton DK, Chao L, Evesson F, He K, Yang PL, et al. (2016). Identification and characterization of a novel broad-spectrum virus entry inhibitor. J. Virol 90, 4494–4510. 10.1128/jvi.00103-16. [PubMed: 26912630]

Cuatrecasas P (1973). Gangliosides and membrane receptors for cholera toxin. Biochemistry 12, 3558–3566. 10.1021/bi00742a032. [PubMed: 4731192]

Day CA, and Kenworthy AK (2012). Mechanisms underlying the confined diffusion of cholera toxin B-subunit in intact cell membranes. PLoS One 7, e34923. 10.1371/journal.pone.0034923. [PubMed: 22511973]

Deng Y, Rivera-Molina FE, Toomre DK, and Burd CG (2016). Sphingomyelin is sorted at the trans Golgi network into a distinct class of secretory vesicle. Proc. Natl. Acad. Sci. U S A 113, 6677–6682. 10.1073/pnas.1602875113. [PubMed: 27247384]

Dirksen A, and Dawson PE (2008). Rapid oxime and hydrazone ligations with aromatic aldehydes for biomolecular labeling. Bioconjug Chem 19, 2543–2548. 10.1021/bc800310p. [PubMed: 19053314]

Doench JG, Fusi N, Sullender M, Hegde M, Vaimberg EW, Donovan KF, Smith I, Tothova Z, Wilen C, Orchard R, et al. (2016). Optimized sgRNA design to maximize activity and minimize off-target effects of CRISPR-Cas9. Nat. Biotechnol 34, 184–191. 10.1038/nbt.3437. [PubMed: 26780180]

Fanani ML, and Maggio B (2017a). The many faces (and phases) of ceramide and sphingomyelin I - single lipids. Biophys. Rev 9, 589–600. 10.1007/s12551-017-0297-z. [PubMed: 28815463]

Fanani ML, and Maggio B (2017b). The many faces (and phases) of ceramide and sphingomyelin II - binary mixtures. Biophys. Rev 9, 601–616. 10.1007/s12551-017-0298-y. [PubMed: 28823080]

Fujimoto T, and Parmryd I (2017). Interleaflet coupling, pinning, and leaflet asymmetry—major players in plasma membrane nanodomain formation. Front. Cell Dev. Biol 4, 155. 10.3389/fcell.2016.00155. [PubMed: 28119914]

Fujita A, Cheng J, and Fujimoto T (2009). Segregation of GM1 and GM3 clusters in the cell membrane depends on the intact actin cytoskeleton. Biochim. Biophys. Acta 1791, 388–396. 10.1016/j.bbalip.2009.01.008. [PubMed: 19830910]

Gajenthra Kumar N, Contaifer D Jr., Baker PRS, Ekroos K, Jefferson KK, and Wijesinghe DS (2018). Untargeted lipidomic analysis to broadly characterize the effects of pathogenic and non-pathogenic staphylococci on mammalian lipids. PLoS One 13, e0206606. 10.1371/journal.pone.0206606. [PubMed: 30379915]

Garcia-Castillo MD, Chinnapen DJF, Te Welscher YM, Gonzalez RJ, Softic S, Pacheco M, Mrsny RJ, Kahn CR, von Andrian UH, Lau J, et al. (2018). Mucosal absorption of therapeutic peptides by harnessing the endogenous sorting of glycosphingolipids. Elife 7, e34469. 10.7554/elife.34469. [PubMed: 29851380]

Garcia-Parajo MF, Cambi A, Torreno-Pina JA, Thompson N, and Jacobson K (2014). Nanoclustering as a dominant feature of plasma membrane organization. J. Cell Sci 127, 4995–5005. 10.1242/jcs.146340. [PubMed: 25453114]

Shawn Goodwin J, Drake KR, Remmert CL, and Kenworthy AK (2005). Ras diffusion is sensitive to plasma membrane viscosity. Biophys. J 89, 1398–1410. 10.1529/biophysj.104.055640. [PubMed: 15923235]

Goswami D, Gowrishankar K, Bilgrami S, Ghosh S, Raghupathy R, Chadda R, Vishwakarma R, Rao M, and Mayor S (2008). Nanoclusters of GPI-anchored proteins are formed by cortical actin-driven activity. Cell 135, 1085–1097. 10.1016/j.cell.2008.11.032. [PubMed: 19070578]

Gowrishankar K, Ghosh S, Saha S, C R, Mayor S, and Rao M (2012). Active remodeling of cortical actin regulates spatiotemporal organization of cell surface molecules. Cell 149, 1353–1367. 10.1016/j.cell.2012.05.008. [PubMed: 22682254]

Hannun YA, and Obeid LM (2018). Sphingolipids and their metabolism in physiology and disease. Nat. Rev. Mol. Cell Biol 19, 175–191. 10.1038/nrm.2017.107. [PubMed: 29165427]

Hao M, Mukherjee S, Sun Y, and Maxfield FR (2004). Effects of cholesterol depletion and increased lipid unsaturation on the properties of endocytic membranes. J. Biol. Chem 279, 14171–14178. 10.1074/jbc.m309793200. [PubMed: 14734557]

Jacobson K, Liu P, and Lagerholm BC (2019). The lateral organization and mobility of plasma membrane components. Cell 177, 806–819. 10.1016/j.cell.2019.04.018. [PubMed: 31051105]

Jaikishan S, Björkbom A, and Slotte JP (2010). Sphingomyelin analogs with branched N-acyl chains: the position of branching dramatically affects acyl chain order and sterol interactions in bilayer membranes. Biochim. Biophys. Acta 1798, 1987–1994. 10.1016/j.bbamem.2010.07.006. [PubMed: 20637720]

Johannes L, Parton RG, Bassereau P, and Mayor S (2015). Building endocytic pits without clathrin. Nat. Rev. Mol. Cell Biol 16, 311–321. 10.1038/nrm3968. [PubMed: 25857812]

Kabbani AM, Raghunathan K, Lencer WI, Kenworthy AK, and Kelly CV (2020). Structured clustering of the glycosphingolipid GM1 is required for membrane curvature induced by cholera toxin. Proc. Natl. Acad. Sci. U S A 117, 14978–14986. 10.1073/pnas.2001119117. [PubMed: 32554490]

Kavaliauskiene S, Nymark CM, Bergan J, Simm R, Sylvänne T, Simolin H, Ekroos K, Skotland T, and Sandvig K (2014). Cell density-induced changes in lipid composition and intracellular trafficking. Cell. Mol. Life Sci 71, 1097–1116. 10.1007/s00018-013-1441-y. [PubMed: 23921715]

Kellie SB, Patel B, Pierce EJ, Pierce J, Critchley DR, and Critchley D (1983). Capping of cholera toxin - ganglioside GM1 complexes on mouse lymphocytes is accompanied by co-capping of alpha-actinin. J. Cell Biol 97, 447–454. 10.1083/jcb.97.2.447. [PubMed: 6684122]

Kihara A (2012). Very long-chain fatty acids: elongation, physiology and related disorders. J. Biochem 152, 387–395. 10.1093/jb/mvs105. [PubMed: 22984005]

Koval M, and Pagano RE (1991). Intracellular transport and metabolism of sphingomyelin. Biochim. Biophys. Acta 1082, 113–125. 10.1016/0005-2760(91)90184-j. [PubMed: 2007175]

Kusumi A, Fujiwara TK, Morone N, Yoshida KJ, Chadda R, Xie M, Kasai RS, and Suzuki KG (2012). Membrane mechanisms for signal transduction: the coupling of the meso-scale raft domains to membrane-skeleton-induced compartments and dynamic protein complexes. Semin. Cell Dev. Biol 23, 126–144. 10.1016/j.semcdb.2012.01.018. [PubMed: 22309841]

Lakshminarayan R, Wunder C, Becken U, Howes MT, Benzing C, Arumugam S, Sales S, Ariotti N, Chambon V, Lamaze C, et al. (2014). Galectin-3 drives glycosphingolipid-dependent biogenesis of clathrin-independent carriers. Nat. Cell Biol 16, 592–603. 10.1038/ncb2970.

Lencer WI, and Tsai B (2003). The intracellular voyage of cholera toxin: going retro. Trends Biochem. Sci 28, 639–645. 10.1016/j.tibs.2003.10.002. [PubMed: 14659695]

Liaw L, Prudovsky I, Koza RA, Anunciado-Koza RV, Siviski ME, Lindner V, Friesel RE, Rosen CJ, Baker PR, Simons B, and Vary CPH (2016). Lipid profiling of in vitro cell models of adipogenic differentiation: relationships with mouse adipose tissues. J. Cell. Biochem 117, 2182–2193. 10.1002/jcb.25522. [PubMed: 26910604]

Lingwood D, and Simons K (2010). Lipid rafts as a membrane-organizing principle. Science 327, 46–50. 10.1126/science.1174621. [PubMed: 20044567]

Lippincott-Schwartz J, and Phair RD (2010). Lipids and cholesterol as regulators of traffic in the endomembrane system. Annu. Rev. Biophys 39, 559–578. 10.1146/annurev.biophys.093008.131357. [PubMed: 20192772]

London E (2005). How principles of domain formation in model membranes may explain ambiguities concerning lipid raft formation in cells. Biochim. Biophys. Acta 1746, 203–220. 10.1016/j.bbamcr.2005.09.002. [PubMed: 16225940]

Lorizate M, Sachsenheimer T, Glass B, Habermann A, Gerl MJ, Kräusslich HG, and Brügger B (2013). Comparative lipidomics analysis of HIV-1 particles and their producer cell membrane in different cell lines. Cell Microbiol 15, 292–304. 10.1111/cmi.12101. [PubMed: 23279151]

Luong P, Li Q, Chen P-F, Wrighton PJ, Chang D, Dwyer S, Bayer M-T, Snapper SB, Hansen SH, Thiagarajah JR, et al. (2020). A quantitative single-cell assay for retrograde membrane traffic enables rapid detection of defects in cellular organization. Mol. Biol. Cell 31, 511–519. 10.1091/mbc.e19-07-0375. [PubMed: 31774722]

Maxfield FR, and McGraw TE (2004). Endocytic recycling. Nat. Rev. Mol. Cell Biol 5, 121–132. 10.1038/nrm1315. [PubMed: 15040445]

Mayor S, Presley JF, and Maxfield FR (1993). Sorting of membrane components from endosomes and subsequent recycling to the cell surface occurs by a bulk flow process. J. Cell Biol 121, 1257–1269. 10.1083/jcb.121.6.1257. [PubMed: 8509447]

Merrill AH Jr. (2011). Sphingolipid and glycosphingolipid metabolic pathways in the era of sphingolipidomics. Chem. Rev 111, 6387–6422. 10.1021/cr2002917. [PubMed: 21942574]

Mukherjee S, Ghosh RN, and Maxfield FR (1997). Endocytosis. Physiol. Rev 77, 759–803. 10.1152/physrev.1997.77.3.759. [PubMed: 9234965]

Mukherjee S, Soe TT, and Maxfield FR (1999). Endocytic sorting of lipid analogues differing solely in the chemistry of their hydrophobic tails. J. Cell Biol 144, 1271–1284. 10.1083/jcb.144.6.1271. [PubMed: 10087269]

Nissim-Rafinia M, and Meshorer E (2011). Photobleaching assays (FRAP & FLIP) to measure chromatin protein dynamics in living embryonic stem cells. J. Vis. Exp, e2696. 10.3791/2696.

Noutsi P, Gratton E, and Chaieb S (2016). Assessment of membrane fluidity fluctuations during cellular development reveals time and cell type specificity. PLoS One 11, e0158313. 10.1371/journal.pone.0158313. [PubMed: 27362860]

Nyholm TKM, Engberg O, Hautala V, Tsuchikawa H, Lin KL, Murata M, and Slotte JP (2019). Impact of acyl chain mismatch on the formation and properties of sphingomyelin-cholesterol domains. Biophys. J 117, 1577–1588. 10.1016/j.bpj.2019.09.025. [PubMed: 31610877]

Pacheco AR, Lazarus JE, Sit B, Schmieder S, Lencer WI, Blondel CJ, Doench JG, Davis BM, and Waldor MK (2018). CRISPR screen reveals that EHEC's T3SS and shiga toxin rely on shared host factors for infection. mBio 9, e01003–e01018. 10.1128/mbio.01003-18. [PubMed: 29921669]

Park JW, Park WJ, and Futerman AH (2014). Ceramide synthases as potential targets for therapeutic intervention in human diseases. Biochim. Biophys. Acta 1841, 671–681. 10.1016/j.bbalip.2013.08.019. [PubMed: 24021978]

Patterson GH, Hirschberg K, Polishchuk RS, Gerlich D, Phair RD, and Lippincott-Schwartz J (2008). Transport through the Golgi apparatus by rapid partitioning within a two-phase membrane system. Cell 133, 1055–1067. 10.1016/j.cell.2008.04.044. [PubMed: 18555781]

Pike LJ (2004). Lipid rafts: heterogeneity on the high seas. Biochem. J 378, 281–292. 10.1042/bj20031672. [PubMed: 14662007]

Raghunathan K, and Kenworthy AK (2018). Dynamic pattern generation in cell membranes: current insights into membrane organization. Biochim. Biophys. Acta Biomembr 1860, 2018–2031. 10.1016/j.bbamem.2018.05.002. [PubMed: 29752898]

Raghunathan K, Wong TH, Chinnapen DJ, Lencer WI, Jobling MG, and Kenworthy AK (2016). Glycolipid crosslinking is required for cholera toxin to partition into and stabilize ordered domains. Biophys. J 111, 2547–2550. 10.1016/j.bpj.2016.11.008. [PubMed: 27914621]

Raghupathy R, Anilkumar AA, Polley A, Singh PP, Yadav M, Johnson C, Suryawanshi S, Saikam V, Sawant SD, Panda A, et al. (2015). Transbilayer lipid interactions mediate nanoclustering of lipid-anchored proteins. Cell 161, 581–594. 10.1016/j.cell.2015.03.048. [PubMed: 25910209]

Ramstedt B, and Slotte JP (1999). Interaction of cholesterol with sphingomyelins and acyl-chain-matched phosphatidylcholines: a comparative study of the effect of the chain length. Biophys. J 76, 908–915. 10.1016/s0006-3495(99)77254-1. [PubMed: 9929492]

Ramstedt B, and Slotte JP (2002). Membrane properties of sphingomyelins. FEBS Lett 531, 33–37. 10.1016/s0014-5793(02)03406-3. [PubMed: 12401199]

Rodriguez-Gallardo S, Kurokawa K, Sabido-Bozo S, Cortes-Gomez A, Ikeda A, Zoni V, Aguilera-Romero A, Perez-Linero AM, Lopez S, Waga M, et al. (2020). Ceramide chain length-dependent

protein sorting into selective endoplasmic reticulum exit sites. Sci. Adv 6, eaba8237. 10.1126/sciadv.aba8237. [PubMed: 33310842]

Róg T, Or1owski A, Llorente A, Skotland T, Sylvänne T, Kauhanen D, Ekroos K, Sandvig K, and Vattulainen I (2016). Interdigitation of long-chain sphingomyelin induces coupling of membrane leaflets in a cholesterol dependent manner. Biochim. Biophys. Acta 1858, 281–288. 10.1016/j.bbamem.2015.12.003. [PubMed: 26654782]

Römer W, Berland L, Chambon V, Gaus K, Windschiegl B, Tenza D, Aly MRE, Fraisier V, Florent JC, Perrais D, et al. (2007). Shiga toxin induces tubular membrane invaginations for its uptake into cells. Nature 450, 670–675. 10.1038/nature05996. [PubMed: 18046403]

Roux A, Cuvelier D, Nassoy P, Prost J, Bassereau P, and Goud B (2005). Role of curvature and phase transition in lipid sorting and fission of membrane tubules. EMBO J 24, 1537–1545. 10.1038/sj.emboj.7600631. [PubMed: 15791208]

Sandvig K (2001). Shiga toxins. Toxicon 39, 1629–1635. 10.1016/s0041-0101(01)00150-7. [PubMed: 11595626]

Saslowsky DE, te Welscher YM, Chinnapen DJF, Wagner JS, Wan J, Kern E, and Lencer WI (2013). Ganglioside GM1-mediated transcytosis of cholera toxin bypasses the retrograde pathway and depends on the structure of the ceramide domain. J. Biol. Chem 288, 25804–25809. 10.1074/jbc.m113.474957. [PubMed: 23884419]

Sezgin E, Kaiser HJ, Baumgart T, Schwille P, Simons K, and Levental I (2012). Elucidating membrane structure and protein behavior using giant plasma membrane vesicles. Nat. Protoc 7, 1042–1051. 10.1038/nprot.2012.059. [PubMed: 22555243]

Sezgin E, Levental I, Mayor S, and Eggeling C (2017). The mystery of membrane organization: composition, regulation and roles of lipid rafts. Nat. Rev. Mol. Cell Biol 18, 361–374. 10.1038/nrm.2017.16. [PubMed: 28356571]

Shaner RL, Allegood JC, Park H, Wang E, Kelly S, Haynes CA, Sullards MC, and Merrill AH Jr. (2009). Quantitative analysis of sphingolipids for lipidomics using triple quadrupole and quadrupole linear ion trap mass spectrometers. J. Lipid Res 50, 1692–1707. 10.1194/jlr.d800051-jlr200. [PubMed: 19036716]

Simons K, and Sampaio JL (2011). Membrane organization and lipid rafts. Cold Spring Harbor Perspect. Biol 3, a004697. 10.1101/cshperspect.a004697.

Simons K, and van Meer G (1988). Lipid sorting in epithelial cells. Biochemistry 27, 6197–6202. 10.1021/bi00417a001. [PubMed: 3064805]

Simons K, and Vaz WL (2004). Model systems, lipid rafts, and cell membranes. Annu. Rev. Biophys. Biomol. Struct 33, 269–295. 10.1146/annurev.biophys.32.110601.141803. [PubMed: 15139814]

Skotland T, and Sandvig K (2019). The role of PS 18:0/18:1 in membrane function. Nat. Commun 10, 2752. 10.1038/s41467-019-10711-1. [PubMed: 31227693]

Sorre B, Callan-Jones A, Manneville JB, Nassoy P, Joanny JF, Prost J, Goud B, and Bassereau P (2009). Curvature-driven lipid sorting needs proximity to a demixing point and is aided by proteins. Proc. Natl. Acad. Sci. U S A 106, 5622–5626. 10.1073/pnas.0811243106. [PubMed: 19304798]

Spillane KM, Ortega-Arroyo J, de Wit G, Eggeling C, Ewers H, Wallace MI, and Kukura P (2014). High-speed single-particle tracking of GM1 in model membranes reveals anomalous diffusion due to interleaflet coupling and molecular pinning. Nano Lett 14, 5390–5397. 10.1021/nl502536u. [PubMed: 25133992]

Steinkühler J, Sezgin E, Urbančič I, Eggeling C, and Dimova R (2019). Mechanical properties of plasma membrane vesicles correlate with lipid order, viscosity and cell density. Commun. Biol 2, 337. 10.1038/s42003-019-0583-3. [PubMed: 31531398]

Stillman BN, Hsu DK, Pang M, Brewer CF, Johnson P, Liu FT, and Baum LG (2006). Galectin-3 and galectin-1 bind distinct cell surface glycoprotein receptors to induce T cell death. J. Immunol 176, 778–789. 10.4049/jimmunol.176.2.778. [PubMed: 16393961]

Stockton GW, and CP Smith I (1976). A deuterium nuclear magnetic resonance study of the condensing effect of cholesterol on egg phosphatidylcholine bilayer membranes. I. Perdeuterated fatty acid probes. Chem. Phys. Lipids 17, 251–263. 10.1016/0009-3084(76)90070-0. [PubMed: 1033045]

Stone MB, Shelby SA, Nunez MF, Wisser K, and Veatch SL (2017). Protein sorting by lipid phase-like domains supports emergent signaling function in B lymphocyte plasma membranes. Elife 6, e19891. 10.7554/elife.19891. [PubMed: 28145867]

te Welscher YM, Chinnapen DJF, Kaoutzani L, Mrsny RJ, and Lencer WI (2014). Unsaturated glycoceramides as molecular carriers for mucosal drug delivery of GLP-1. J. Contr. Release 175, 72–78. 10.1016/j.jconrel.2013.12.013.

van Meer G, and Simons K (1982). Viruses budding from either the apical or the basolateral plasma membrane domain of MDCK cells have unique phospholipid compositions. EMBO J 1, 847–852. 10.1002/j.1460-2075.1982.tb01258.x. [PubMed: 6329709]

van Meer G, Voelker DR, and Feigenson GW (2008). Membrane lipids: where they are and how they behave. Nat. Rev. Mol. Cell Biol 9, 112–124. 10.1038/nrm2330. [PubMed: 18216768]

Varshney P, Yadav V, and Saini N (2016). Lipid rafts in immune signalling: current progress and future perspective. Immunology 149, 13–24. 10.1111/imm.12617. [PubMed: 27153983]

Veatch SL, et al. (2003). Separation of liquid phases in giant vesicles of ternary mixtures of phospholipids and cholesterol. Biophys J 10.1016/S0006-3495(03)74726-2.

Wolf AA, Jobling MG, Saslowsky DE, Kern E, Drake KR, Kenworthy AK, Holmes RK, and Lencer WI (2008). Attenuated endocytosis and toxicity of a mutant cholera toxin with decreased ability to cluster ganglioside GM_1 molecules. Infect. Immun 76, 1476–1484. 10.1128/iai.01286-07. [PubMed: 18212085]

Young WW, Lutz MS, and Blackburn WA (1992). Endogenous glycosphingolipids move to the cell surface at a rate consistent with bulk flow estimates. J. Biol. Chem 267, 12011–12015. 10.1016/s0021-9258(19)49798-6. [PubMed: 1601871]

Zhou Y, and Hancock JF (2015). Ras nanoclusters: versatile lipid-based signaling platforms. Biochim. Biophys. Acta 1853, 841–849. 10.1016/j.bbamcr.2014.09.008. [PubMed: 25234412]

Highlights

- Glycosphingolipids are sorted by a C14* motif in fatty acid of the ceramide
- C14* motif consists of 14 plus 1 saturated hydrocarbons extending from the amide bond
- Glycosphingolipids with C14* motif are exclusively sorted to lysosome
- Sorting by C14* motif is cholesterol dependent

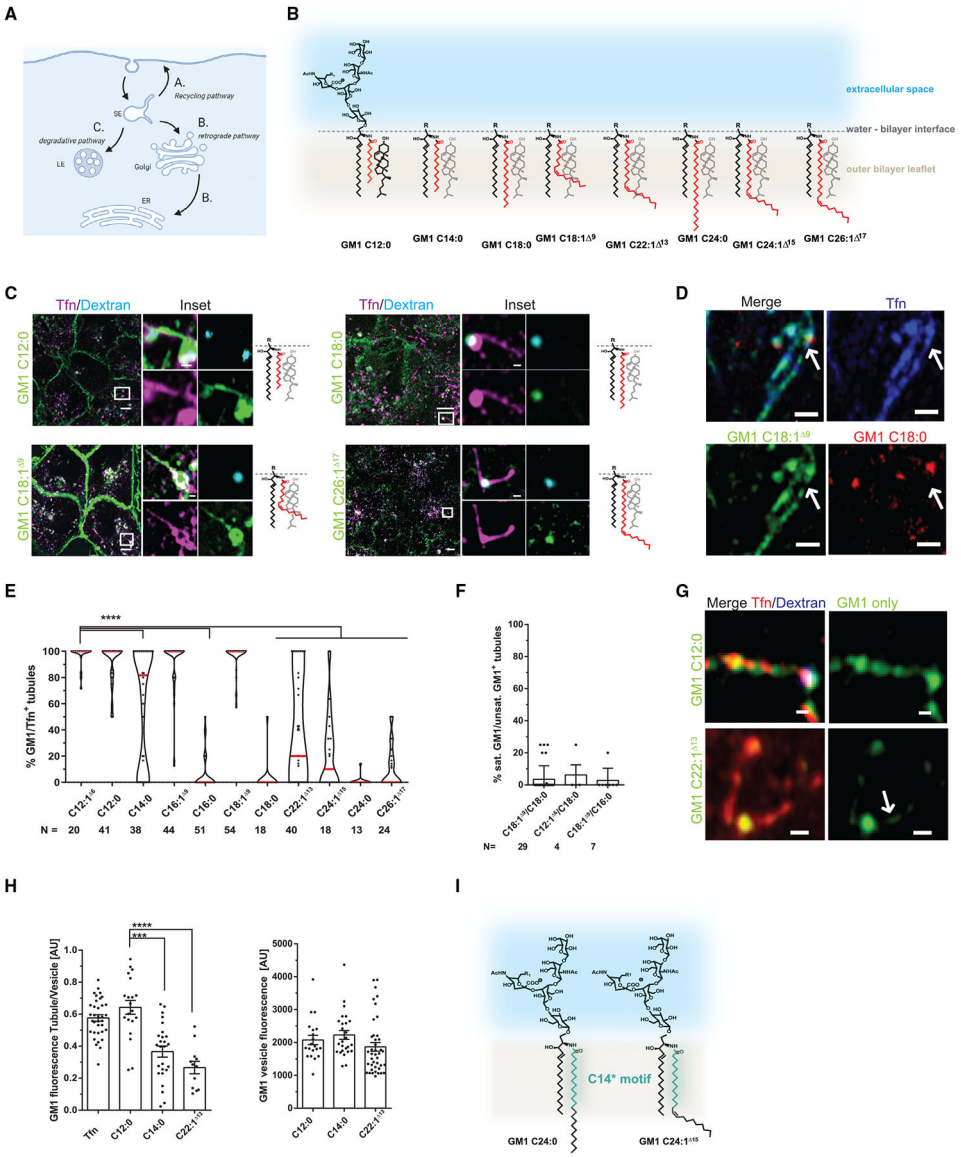

Figure 1. Ceramide structure-specific trafficking within the sorting endosome (SE)

(A) Schematic of endocytic pathways emerging from the SE. Both the recycling and retrograde pathways (marked A and B) require sorting into narrow endosomal tubules. Cargoes destined for degradation are retained within the sorting endosomal body for maturation to late endosomes (LEs) (marked C).

(B) Library of GM1 species synthesized acyl chains marked in red and arbitrarily aligned against cholesterol to highlight changes in acyl chain structure. GM1 C12:1$^{\Delta 6}$, C16:0, and GM1 C16:1$^{\Delta 9}$ species not shown.

(C) Airyscan live cell imaging of recycling endosomal vesicles in A431 epithelial cells, marked by co-localization between transferrin (Tfn) (magenta) and dextran (turquoise). GM1 species in green. Scale bars, 5 and 0.5 μm, respectively.

(D) Same as (C) for cells concomitantly treated with GM1 C18:1$^{\Delta 9}$ (green) and GM1 C18:0 (red). Scale bar, 1 μm.

(E) Quantification of GM1 presence in Tfn marked recycling endosomal tubules. Means ± SEMs, ****$p \leq 0.0001$ by 1-way ANOVA and Tukey's multiple comparison using GM1 C12:0 as comparison; N, total number of regions of interest (ROIs) analyzed.
(F) Co-localization of GM1 C18:0 or C16:0 with GM1 C18:$1^{\Delta 9}$ or C12:$1^{\Delta 6}$ species, respectively, in recycling Tfn^{+} endosomal tubules. Quantification and statistics as in (E).
(G) Recycling tubules analyzed as in (C) using GM1 C22:$1^{\Delta 13}$ and GM1 C12:0 species (green), Tfn (red). Scale bar, 0.5 μm.
(H) Left panel: Quantification of mean gray values of GM1 fluorescence in Tfn tubule normalized to GM1 fluorescence in body of recycling endosomes for GM1 C12:0, C14:0, and C22:$1^{\Delta 13}$. Right panel: Mean gray value of GM1 fluorescence in body of recycling endosome for the same GM1 species. Means ± SEMs. ****$p \leq 0.0001$ against GM1 C12:0 by 1-way ANOVA and Tukey's multiple comparison.
(I) The C14* motif in the acyl chain is 14 saturated hydrocarbons plus 1 in length, extending from the C1 amide bond at the water-bilayer interface. GM1 C24:0 and GM1 C24:$1^{\Delta 15}$, with the C14* motif in acyl chain in turquoise.

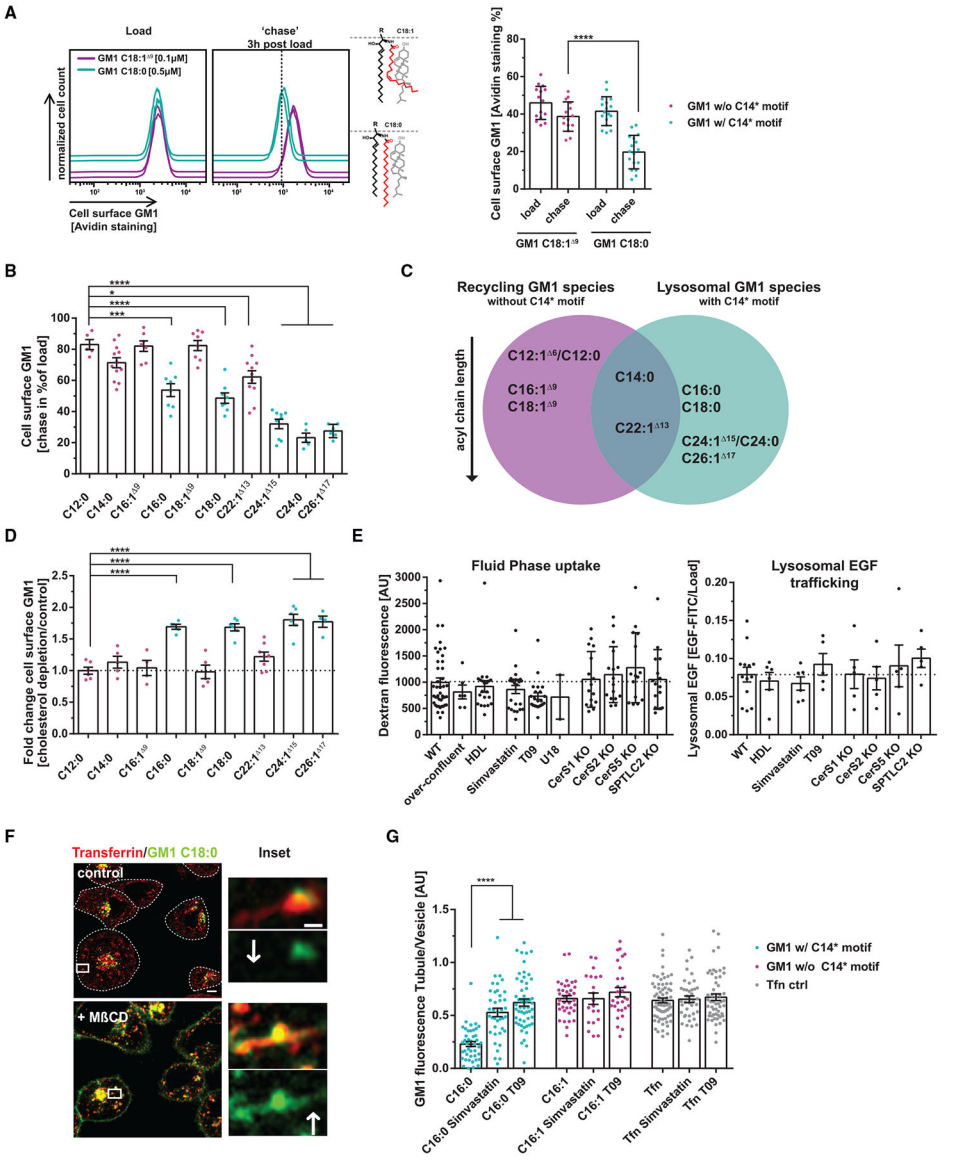

Figure 2. C14* motif dictates differential sorting between the lysosomal and recycling pathways

(A) PM concentrations of GM1 C18:0 (turquoise, with C14* motif) and GM1 C18:1$^{\Delta 9}$ (magenta, without C14* motif) as assessed by FACS using AlexaFluor-labeled streptavidin immediately after loading and after a 3-h chase. Quantification (right panel) with means ± SEMs, each dot equals 2 biological replicates measuring 20,000 cells each. ****p ≤ 0.0001 by unpaired t test.

(B) PM recycling as in (A) for the GM1 structural library (GM1 species with C14* motif in turquoise, GM1 species without C14* motif in magenta). Means ± SEMs. One-way ANOVA and Tukey's multiple comparison.

(C) Venn diagram for ceramide acyl chain structure-dependent GM1 sorting in the endosomal system. Recycling GM1 species without C14* motif are in magenta and GM1 species entering the lysosomal pathway containing the C14* motif are in turquoise.

(D) Change in recycling rates under mildly cholesterol-depleting conditions (simvastatin treatment, 24 h, 10 μM). Recycling assay as in (A). ****$p \leq 0.0001$ by 1-way ANOVA and Tukey's multiple comparison.

(E) Fluid phase uptake by fluorescent dextran (left) and lysosomal trafficking of EGF (right) measured by FACS in A431 cells depleted or not of cholesterol as indicated (growth to over-confluency, growth in high-density lipoprotein (HDL)-depleted serum, 10 μM simvastatin, 100 nM T0901317 for 24 h, 1 μg/mL U18666A for 12 h, or using the respective CRISPR-Cas9 KO line). No differences were observed as measured by 1-way ANOVA and Tukey's multiple comparison.

(F) Images of Tfn recycling tubules (red) in A431 cells treated or not with 2.5 mMβCD and GM1 C18:0 (green). Scale bars, 5 and 0.5 μm, respectively.

(G) Entry of GM1 C16:0 or C16:$1^{\Delta 9}$ into recycling tubules in cholesterol-depleted A431 cells as indicated. Mean gray values of fluorescent GM1 in both endosomal vesicle and tubule were recorded, and the ratio of GM1 fluorescence in tubule over vesicle was calculated for each condition. Each dot represents one tubule versus vesicle ratio. Means ± SEMs. ****$p \leq 0.0001$ by 1-way ANOVA and Tukey's multiple comparison.

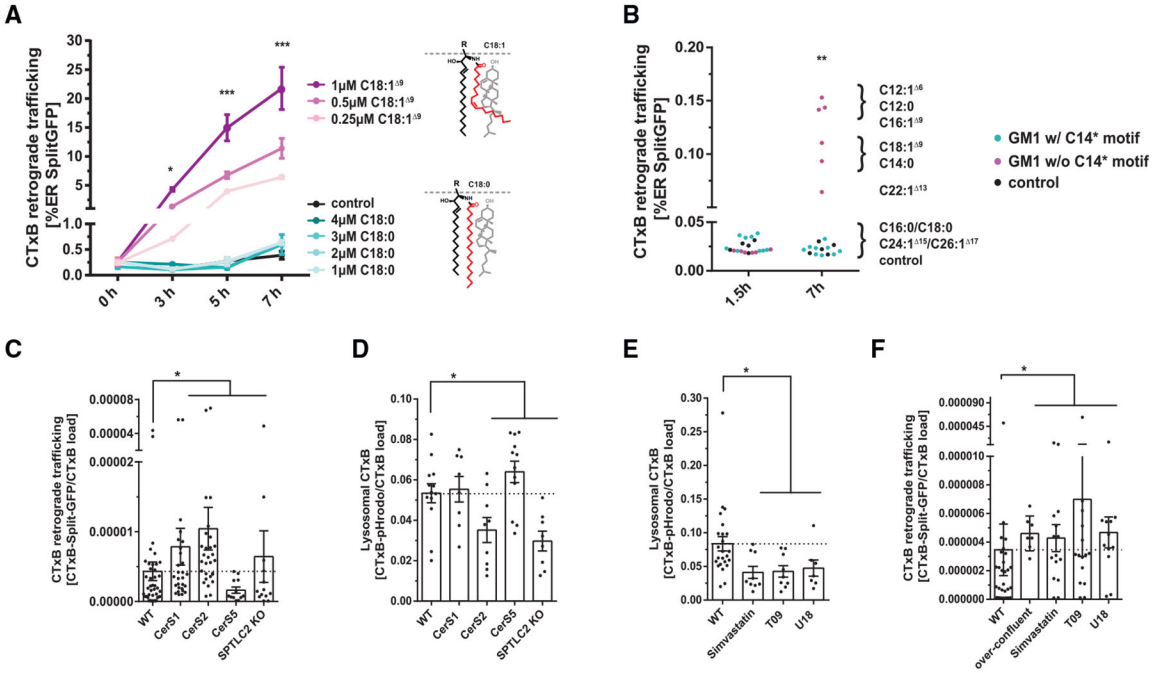

Figure 3. Ceramide-dependent sorting into the retrograde pathway

(A) Time course of retrograde GM1 trafficking to the ER by a SplitGFP-based FACS assay in a GM1^{-} HeLa cell line using different concentrations of GM1 C18:1$^{\Delta 9}$ (magenta) and GM1 C18:0 (turquoise). Graph dots represent the means ± SDs of 2 biological replicates measuring 20,000 cells each. ****p ≤ 0.0001 by 1-way ANOVA and Tukey's multiple comparison.

(B) SplitGFP assay as in (A) loaded with different GM1 species. Graph dots represent the means ± SEMs of 2 biological replicates measuring 20,000 cells each.

(C) A431 CRISPR-Cas9 KO cell lines for different ceramide synthases stably expressing ER-SplitGFP. SplitGFP signal after 5 h is normalized to fluorescent CTxB surface binding. Dots represent mean of 3 biological replicates. Means ± SEMs. ****p ≤ 0.0001 by 1-way ANOVA and Tukey's multiple comparison.

(D) FACS assay measuring lysosomal transport of GM1-CTxB-pHrodo in A431 CRISPR-Cas9 KO cell lines for different ceramide synthases. Lysosomal pHrodo signal after 1 h is normalized to fluorescent CTxB surface binding. Dots represent mean of 3 biological replicates of 20,000 cells each. Means ± SEMs. ****p ≤ 0.0001 by 1-way ANOVA and Tukey's multiple comparison.

(E) Lysosomal transport of GM1-CTxB-pHrodo in A431 WT cells as in (D) mildly depleted of cholesterol as indicated, with simvastatin (10 μM) and T0901317 (100 nM) 24 h before or U18666A (1 μg/mL) 12 h before experiment. Dots represent mean of 3 biological replicates measuring 20,000 cells each. Means ± SEMs. ****p ≤ 0.0001 by 1-way ANOVA and Tukey's multiple comparison.

(F) A431 WT cells were mildly depleted of cholesterol as in (E), and retrograde transport was measured as in (C). Dots represent mean of 3 biological replicates measuring 20,000 cells each. Means ± SEMs. ****p ≤ 0.0001 by 1-way ANOVA and Tukey's multiple comparison.

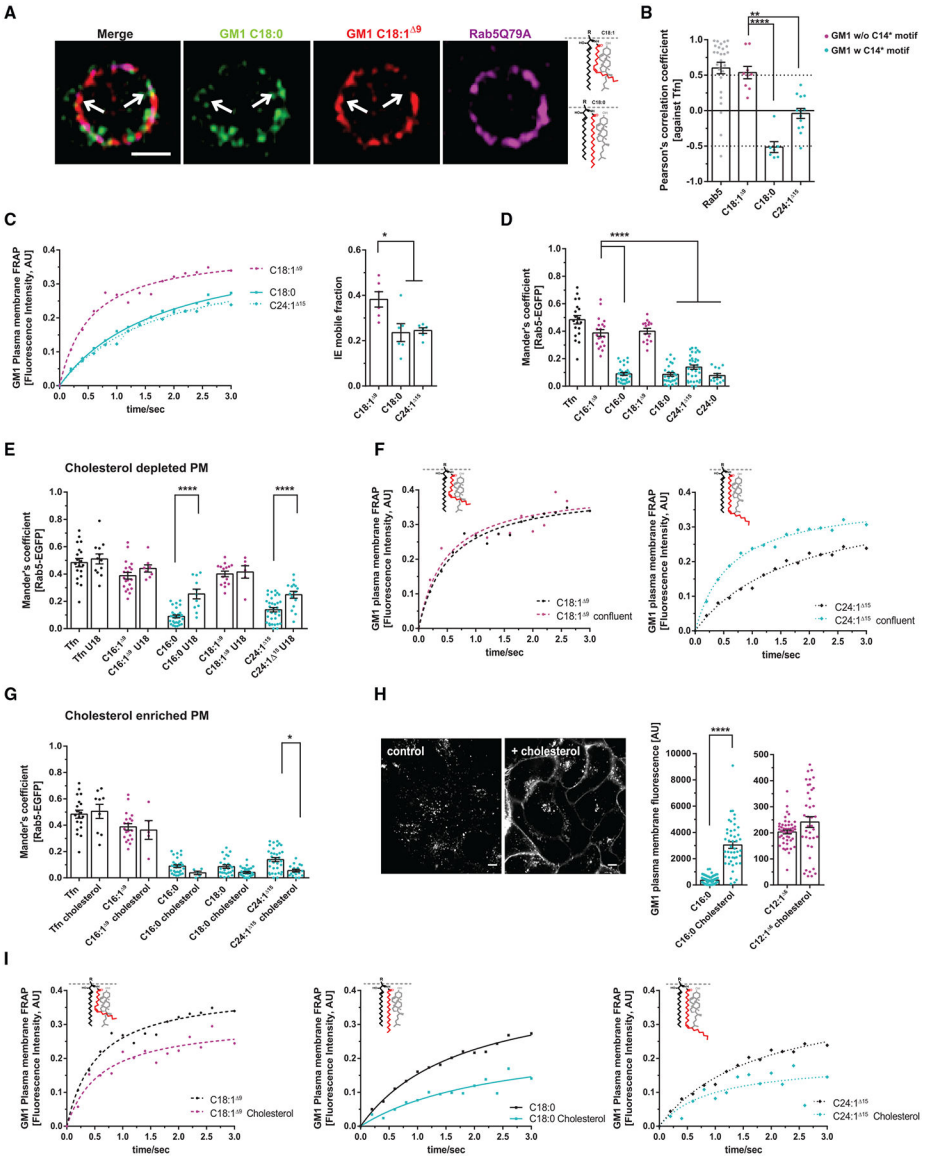

Figure 4. C14* motif drives GM1 segregation in endosomes and at the PM

(A) GM1 C18:0 (green) and GM1 C18:1$^{\Delta 9}$ (red) were incorporated into A431 cells transfected with dominant active RAB5Q79L-GFP plasmid (magenta). Scale bar, 1 μm.

(B) Pearson's correlation coefficient against Tfn. Dots represent Pearson's correlation coefficient for 1 enlarged RAB5 early endosome. GM1 species with C14* motif are displayed in turquoise and GM1 species without C14* motif in magenta. ****p ≤ 0.0001 by 1-way ANOVA and Tukey's multiple comparison.

(C) A431 WT cells were incorporated with the respective GM1 species, and a PM ROI was photobleached immediately. Left panel: Fluorescence recovery after bleaching (FRAP) was recorded and mean gray values of 1 representative experiment are displayed. Right panel: Quantification of end value of the recovered fluorescence intensity mobile fraction for FRAP experiments. Dots represent mean gray fluorescence for 1 FRAP experiment. Means ± SEMs. ****p ≤ 0.0001 by 1-way ANOVA and Tukey's multiple comparison.

(D) Fluorescently labeled GM1 species were incorporated into genome-edited SVGA cells expressing RAB5-EGFP. GM1-RAB5-EGFP double-positive vesicles were quantified after 5–10 min. Mander's co-localization coefficient was calculated. Means ± SEMs. ****$p \leq 0.0001$ by 1-way ANOVA and Tukey's multiple comparison.
(E) As in (D), but SVGA cells were mildly cholesterol-depleted U18666A [1 μg/mL] 12 h before experiment. ****$p \leq 0.0001$ by 1-way ANOVA and Tukey's multiple comparison.
(F) As in (C), but A431 cells were grown to over-confluency for 48 h before experiment.
(G) As in (D), but to genome-edited SVGA cells 120 μg/mL exogenous cholesterol:MβCD was added for 15 min before imaging. Means ± SEMs. ****$p \leq 0.0001$ by 1-way ANOVA and Tukey's multiple comparison.
(H) Left panel: GM1 C16:0 was incorporated into A431 cells and imaged 30 min post-loading in control cells or cells treated with 120 μg/mL cholesterol:MβCD. Maximum intensity projection; scale bar, 5 μm. Right panel: Quantification of PM fluorescence of GM1 C16:0 and C12:1$^{\Delta 6}$ incorporated into HT29 WT cells untreated or treated with exogenous cholesterol. Mean gray values of cell outlines for GM1 fluorescence were measured. Dots represent mean gray fluorescence for 1 cell outline. Means ± SEMs. ****$p \leq 0.0001$ by 1-way ANOVA and Tukey's multiple comparison.
(I) As in (C), but A431 cells were treated with 120 μg/mL exogenous cholesterol:MβCD.

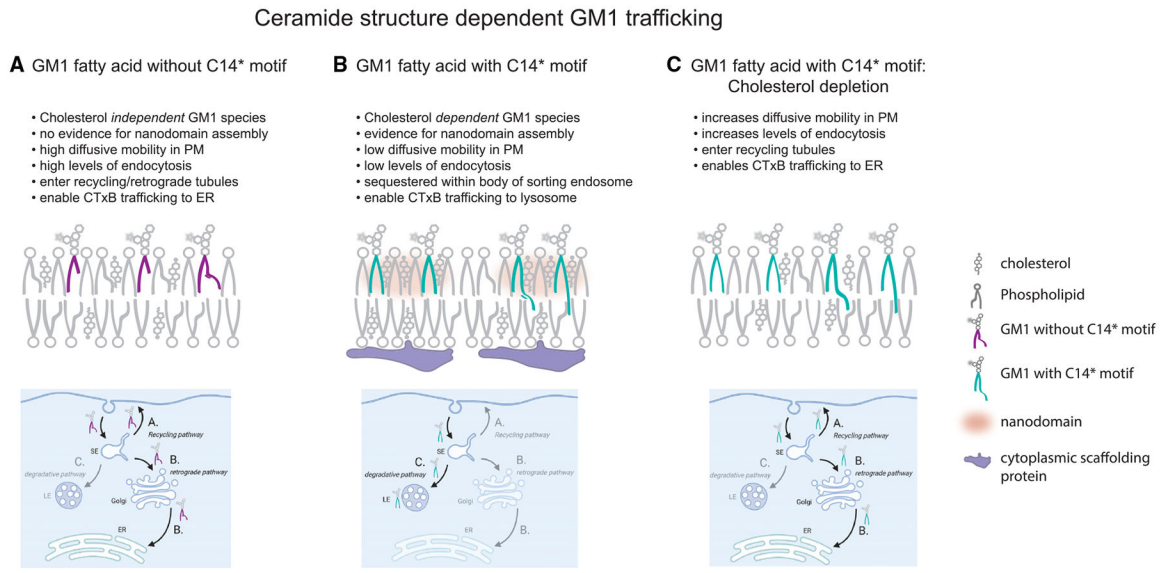

Figure 5. Model for cholesterol-ceramide structure-based GM1 sorting

(A) GM1 species with short or unsaturated acyl chains (≤C14:0 or C22:1$^{\Delta 13}$) lacking the C14* motif (magenta) are unable to assemble with cholesterol into membrane nanodomains. Their membrane and endocytic trafficking phenotypes are independent of membrane cholesterol.

(B) GM1 species with long or very long unsaturated acyl chains (≥C16:0 and C24:1$^{\Delta 15}$) containing the C14* motif (turquoise) allow for close packing with cholesterol and therefore assembly into membrane nanodomains (or rafts).

(C) In the absence of cholesterol, GM1 species with C14* motif change their intracellular trafficking behavior, now resembling that of GM1 species lacking the C14* motif.

KEY RESOURCES TABLE

REAGENT or RESOURCE	SOURCE	IDENTIFIER
Bacterial and virus strains		
E. coli Max Efficiency DH10B	Thermo Fisher	18297010
Chemicals, peptides, and recombinant proteins		
GM1 species	This study	10.17632/bk7cmygrdr.1
Dimethylformamide (DMF)	Sigma Aldrich	227056
Dimethylsulfoxide (DMSO)	Sigma Aldrich	472301
Methanol	Fisher Scientific	A456–500
Ethanol	Fisher Scientific	BP28184
Acetonitrile	Fisher Scientific	A955–4
TCEP	Sigma Aldrich	C4706
soluble cholesterol complexed to MβCD	Sigma Aldrich	C4951
defatted bovine serum albumin (dfBSA)	Sigma Aldrich	A8806
fetal bovine serum depleted of HDL (HDL-)	Kalen Biomedical	880100
Simvastatin (statin)	Sigma Aldrich	S6196
T0901317	Sigma Aldrich	T2320
U18666A	Tocris	1638
Filipin III	Sigma Aldrich	F4767
Laurdan	Thermo Fisher	D250
DMEM	Thermo Fisher	12430112
Opti-MEM	Thermo Fisher	51985091
Lipofectamine 2000	Thermo Fisher	11668030
*FAST*Dil™	Thermo Fisher	D7756
*FAST*Dio™	Thermo Fisher	D3898
Alexa Fluor™ 488 Azide (also 568 and 647)	Thermo Fisher	A10266
pHrodo™ Green Epidermal Growth Factor	Thermo Fisher	P35375
pHrodo™ Red Transferrin Conjugate (also–AlexaFluor 488, 568, 647)	Thermo Fisher	P35376
pHrodo™ iFL Green STP Ester	Thermo Fisher	P36012
Dextran, Cascade Blue™, 3000 MW (also−488)	Thermo Fisher	D7132
LysoTracker™ Red DND-99 (also DND-22)	Thermo Fisher	L7528
Blasticidin	Thermo Fisher	A1113903
Puromycin	Sigma-Aldrich	540411
Hygromycin	Thermo Fisher	10687010
Experimental models: Cell lines		
A431 WT	ATCC	CRL-1555
A431 SPTLC-2 KO	This study	N/A
A431 UGCG KO	This study	N/A
A431 CerS1	This study	N/A
A431 CerS2 KO	This study	N/A

REAGENT or RESOURCE	SOURCE	IDENTIFIER
A431 CerS5	This study	N/A
HT29 Cas9	Pacheco et al.	Pacheco et al., 2018
Hela WT	ATCC	CRM-CCL-2
HEK293T	ATCC	ACS-4500
CaCo BBE WT		
SVGA Rab5-GFP	Chou et al.	Chou et al., 2016
Oligonucleotides		
SPTLC-2 ACAACTATCTTGGATTTGCA	Pacheco et al.	Pacheco et al., 2018
UGCG ACAACTATCTTGGATTTGCA	Pacheco et al.	Pacheco et al., 2018
CerS1 AGCGCTCTCGGGCATCTTGG GCTTCCCTGGAGCAGGTAGG GCAGCCGCCTACCTGCTCCA TACGCGCAGCTAGTGCAGCG	This study	N/A
CerS2 GCTGCCTGTGAACTTGACCT TTCTTCATGTCATAGAACCA GGTCAGGTAGAAATGTTCCA GTAAAATGTGAATCTCCAGC	This study	N/A
CerS5 GTATCCTGATAAGAAAAGGC TGATGAAACCAAGACCCAAG ATGCCAATACAGAGTGCACA ATAAAATGTGAATCTCCACC	This study	N/A
Recombinant DNA		
packaging plasmids pVSVg	Addgene	#8454
packaging plasmids psPAX2	Addgene	#12260
lentiCas9-Blast plasmid	Addgene	#52962
lentiGuide-Puro plasmid	Addgene	#52963
dominant active RAB5Q79L-GFP plasmid	Addgene	#28046
dominant active RAB5Q79L-GFP plasmid	Addgene	#35138
Software and algorithms		
ZENblack	Zeiss	https://www.zeiss.com/microscopy/us/products/microscope-software/zen.html
Fiji		https://fiji.sc/
Aivia 9	Drvision Technologies	N/A
Matlab	MathWorks	https://www.mathworks.com/products/matlab.html
Graphpad Prism	Graphpad Prism	https://www.graphpad.com
Other		
Lipidomics profiling	This study	Available upon request from lead contact